

# Confirmation of the VeLLO L1148–IRS: Star Formation at very low (Column) Density

J. Kauffmann<sup>1\*</sup>, F. Bertoldi<sup>2</sup>, T.L. Bourke<sup>3</sup>, P.C. Myers<sup>3</sup>, C.W. Lee<sup>4</sup>, T.L. Huard<sup>5</sup>

<sup>1</sup>NPP Fellow, Jet Propulsion Laboratory, California Institute of Technology, 4800 Oak Grove Drive, Pasadena, CA 91109, USA

<sup>2</sup>Argelander Institut für Astronomie, Universität Bonn, Auf dem Hügel 71, 53121 Bonn, Germany

<sup>3</sup>Harvard-Smithsonian Center for Astrophysics, 60 Garden Street, Cambridge, MA 02138, USA

<sup>4</sup>Korea Astronomy and Space Science Institute, 61–1 Hwaam-dong, Yuseong-gu, Daejeon 305–348, Korea

<sup>5</sup>Department of Astronomy, University of Maryland, College Park, MD 20742, USA

Accepted XXX. Received YYY; in original form ZZZ

## ABSTRACT

We report the detection of a compact ( $\sim 5''$ ; about 1800 AU projected size) CO outflow from L1148–IRS. This confirms that this Spitzer source is physically associated with the nearby ( $\approx 325$  pc) L1148 dense core. Radiative transfer modeling suggests an internal luminosity of 0.08 to  $0.13 L_{\odot}$ . This validates L1148–IRS as a Very Low Luminosity Object (VeLLO;  $L \leq 0.1 L_{\odot}$ ). The L1148 dense core has unusually low densities and column densities for a star-forming core. It is difficult to understand how L1148–IRS might have formed under these conditions. Independent of the exact final mass of this VeLLO (which is likely  $< 0.24 M_{\odot}$ ), L1148–IRS and similar VeLLOs might hold some clues about the isolated formation of brown dwarfs.

**Key words:** stars: formation; stars: low-mass, brown dwarfs; ISM: globules; ISM: individual: L1148; ISM: jets and outflows; infrared: stars

## 1 INTRODUCTION

The sensitivity of the Spitzer Space Telescope allows for searches and studies of young stellar objects that are much less luminous than those studied before. While surveys of star-forming regions using data from the Infrared Astronomical Satellite (IRAS) were sensitive to sources with luminosities  $\gtrsim 0.1 L_{\odot}$  ( $d/140$  pc)<sup>2</sup> (where  $d$  is the distance; Myers et al. 1987), Spitzer can detect objects with luminosities as low as  $4 \times 10^{-3} L_{\odot}$  ( $d/140$  pc)<sup>2</sup>, i.e. has a sensitivity better by a factor 25 (Dunham et al. 2008). Spitzer has imaged a large number of isolated dense cores thought to be starless. About 60 of them were observed as part of the Spitzer Legacy Project “From Molecular Cores to Planet Forming Disks”, or c2d (Evans et al. 2003).

These observations led to a series of discoveries of Very Low Luminosity Objects (VeLLOs; for definitions see Kauffmann et al. 2005, di Francesco et al. 2007, Dunham et al. 2008), infrared stars of luminosity  $\leq 0.1 L_{\odot}$  which are embedded in dense cores. VeLLO colors and envelope properties are consistent with those of class 0 or class I protostars (Lada 1987; André et al. 1993), young stars in their main accretion phase that are deeply embedded in the dense core from which they form.

Young et al. (2004) presented the first Spitzer-identified VeLLO, L1014–IRS (also see: Crapsi et al. 2005b; Huard et al. 2006; Bourke et al. 2005). Further detailed studies were presented

for L1521F–IRS (Bourke et al. 2006) and L328–IRS (Lee et al. 2009). These papers established the initial VeLLO sample and the first overviews of their properties. Other well-studied VeLLO candidates are Cha–MMS1 (Belloche et al. 2006) and L673–7–IRS (Dunham et al. 2010a). See Table 2 for an up-to-date list. The combined c2d survey data for cores and clouds reveals 15 candidate VeLLOs (Dunham et al. 2008). Not all of them are well studied, though. The first VeLLO ever discovered was IRAM04191. It was identified by André et al. (1999) on the basis of millimeter radio observations (see Dunham et al. 2006 for Spitzer results).

The evolutionary status and fate of VeLLOs is presently unclear and likely to be diverse. There is probably general consent that VeLLOs have a present-day mass  $< 0.1 M_{\odot}$  (Young et al. 2004; also see Section 6.1). However, some VeLLOs drive prominent outflows, and thus seem to accrete significantly. These objects have been interpreted as very young ( $\sim 10^4$  yr) protostars of stellar final mass (e.g., IRAM04191, which has a prominent outflow; André et al. 1999; Belloche et al. 2002). In contrast, VeLLOs devoid of such outflows might not accrete at a high rate. Some were proposed to be proto brown dwarfs forming in isolation (i.e., not as low-mass components of clusters and binaries; e.g., L1014–IRS, which has a  $\sim 3''$  [ $\sim 750$  AU] outflow only detected with interferometers; Young et al. 2004; Crapsi et al. 2005b; Bourke et al. 2005; Huard et al. 2006). This concept has been bolstered by recent discoveries of binary brown dwarfs which are too loosely bound to have been expelled by multiple stellar systems (e.g., Radigan et al. 2009 and Luhman et al.

\* E-mail: jens.kauffmann@jpl.nasa.gov

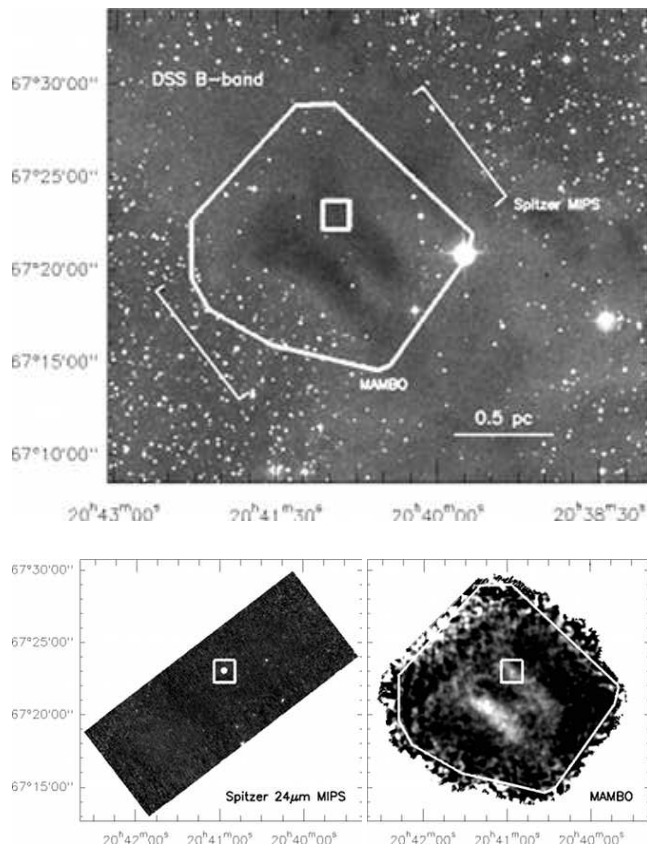


**Figure 1.** The discovery of L1148-IRS. The L1148 region contains two dark dust features evident at optical wavelength (top panel). These are also detected in maps of dust continuum emission (bottom right panel). At  $24\ \mu\text{m}$  wavelength, the source L1148-IRS (framed by a box in all panels) manifests as an unusually bright point source (bottom left panel). It resides near a relatively faint (9 mJy per  $11''$  beam at  $1.2\ \text{mm}$  wavelength after smoothing to  $20''$  resolution) dust continuum emission peak (bottom right panel). Solid and dotted lines indicate the relative orientation of the different maps. See Figure 2 for further information. Coordinates are given for J2000.

2009; also see `\protect\vrule width0pt\protect\href{http://www.vlmbinaries.org/}{http://www.vlmbinaries.org/}`).

The second Spitzer VeLLO to be discovered — the source discussed in the present paper, L1148-IRS (Kauffmann et al. 2005; first noticed by Kun 1998) — always maintained a peculiar status. As shown in Figure 1, this object was discovered as an unusually bright Spitzer MIPS source (compared to the field stars), SSTc2d J204056.66+672304.9, which is closely associated with a  $1.2\ \text{mm}$  wavelength dust emission peak revealed by the c2d MAMBO survey (Kauffmann et al. 2008). It differs from other VeLLOs in that no other such object is as inconspicuous in dust emission (Kauffmann et al. 2005, 2008; Wu et al. 2007). This implies that L1148-IRS resides in a natal dense core of unusually low mass and average density ( $\sim 0.15\ M_{\odot}$ , few  $10^4\ \text{cm}^{-3}$ ; Kauffmann et al. 2008).

Unfortunately, initial single-dish searches by Kauffmann et al. (2005) did not reveal any molecular outflow. Thus, Kauffmann et al. (2005) could not entirely rule out that L1148-IRS is just a galaxy (probability  $\sim 10^{-4}$ , using  $24\ \mu\text{m}$  source counts by Papovich et al. 2004) or background protostar accidentally aligned with the L1148 dense core. Formally, this

means that L1148-IRS does not meet all of the Dunham et al. (2008) criteria for confirmed VeLLOs. Confirmation would require an outflow detection towards L1148-IRS at the systemic velocity of the dense core. This would prove that L1148-IRS (i) is a YSO which is (ii) physically associated with the L1148 region. Here, we present an outflow meeting these criteria.

Our study is organized as follows. Section 2 introduces the data on which our study is based. We discuss the discovery and characterization of the outflow in Section 3. The physical properties of the embedded YSO are derived in Section 4. Information on various VeLLO natal cores are summarized in Section 5. This provides a catalogue against which L1148 can be compared. In Section 6 we turn to a discussion of L1148-IRS in the context of other VeLLOs. Section 7 summarizes our study.

In order to improve the readability of this paper, some complementary material is removed to two appendices. Appendix A provides details on the photometric data used in this study. Appendix B comprehensively presents data for which a cursory analysis was executed in previous studies (i.e., Kauffmann et al. 2005), and describes new data indirectly supporting the outflow analysis executed here.

## 2 DATA & OBSERVATIONS

### 2.1 Distance & Previous Studies

Straizys et al. (1992) derive a distance of  $(325 \pm 25)\ \text{pc}$  for the L1148 region. This is smaller than the  $450\ \text{pc}$  estimated by Kun (1998). We adopt the result by Straizys et al. (1992), since they focus on a  $\leq 1^\circ \times 1^\circ$  field centered on L1148, while Kun (1998) study an  $\approx 2^\circ \times 10^\circ$  region in which L1148 lies only at the edge. This is consistent with a preliminary 2MASS-based distance estimate of  $(301 \pm 55)\ \text{pc}$  (G. Maheswar & C.W. Lee, in prep.; based on Maheswar et al. 2010).

The L1148 dense core was included in the Lee et al. (1999, 2001, 2004) surveys for inward motions. No signs of such motions were found, but the observed lines were weak and the position of L1148-IRS was not probed. Kirk et al. (2005) observed L1148 with SCUBA at  $450\ \mu\text{m}$  and  $850\ \mu\text{m}$  wavelength, but their small target field ( $\approx 2'$  diameter) did not include the VeLLO candidate considered here. The L1148-IRS source was then presented by Kauffmann et al. (2005). Wu et al. (2007) did observe this source with SHARC-II at  $350\ \mu\text{m}$  wavelength, but failed to detect it. These data, combined with the characteristics of the Spitzer-detected source, led Dunham et al. (2008) to the conclusion that L1148-IRS “has a high likelihood of being an embedded low-luminosity protostar” (their ‘group 3’). The source is also included in the  $1.8\ \text{cm}$  radio continuum surveys by Scaife et al. (2010). L1148-IRS is detected at a signal-to-noise ratio  $\sim 3$ . As shown by Scaife et al., and repeated in Table 2, the implied intrinsic luminosity at  $1.8\ \text{cm}$  wavelength is comparable to what is found for other VeLLOs (i.e.  $F_{1.8\text{cm}} d^2$ , the product of observed flux density and distance squared).

Most recently, Kirk et al. (2009) used data from the Spitzer Gould Belt Legacy survey to search the entire L1148 region for young stellar objects (YSOs). Just a single candidate YSO, i.e. our L1148-IRS, is found. This dearth of YSOs is confirmed by Dunham et al. (2008), though they find one further candidate with rather low YSO probability (i.e., in their ‘group 6’). Like neighboring clouds, L1148 does thus form stars only at a very small rate or efficiency (Kirk et al. 2009). Nutter et al. (2009) took Akari data

at wavelength of 65 to 160  $\mu\text{m}$  towards a  $\sim 0.5^\circ \times 0.5^\circ$  field containing L1148–IRS. They detect and confirm L1148–IRS; they do, however, focus on the extended matter in this region and uncover evidence for external heating of the clouds.

Detailed assessments of the properties of the natal dense core of VeLLOs were first presented by Kauffmann et al. (2005). Based on maps in lines of CCS (from the the Effelsberg 100m–telescope) and  $\text{N}_2\text{H}^+$  (from the IRAM 30m–telescope), the dense core has line widths at half intensity  $\lesssim 0.25 \text{ km s}^{-1}$ . Non–thermal motions are thus sub–sonic, since  $\text{H}_2$  at 10 K temperature has a line width of  $0.44 \text{ km s}^{-1}$ . Towards L1148–IRS,  $\text{N}_2\text{H}^+$  lines yield a systemic velocity of  $2.60 \text{ km s}^{-1}$ . Significant velocity gradients and jumps, as well as multiple velocity components in  $\text{C}^{18}\text{O}$ , are observed near the YSO. The letter by Kauffmann et al. (2005) unfortunately lacked the space to present the data in detail. These are therefore for the first time provided in Appendix B.

Based data from the IRAM 30m–telescope, Kauffmann et al. (2005) found no indications for significant chemical evolution. Specifically, CO is depleted by a factor less than 10, and  $\text{N}_2\text{D}^+$  is not detected. See Appendix B4 for more details. However, there is evidence for contraction motions within L1148: line asymmetries indicative of such motions are observed towards all three positions highlighted in Fig. 2. These new data are presented in Appendix B5.

The Kauffmann et al. (2008) dust emission maps (obtained using MAMBO at the IRAM 30m–telescope) reveal an unusually small mass reservoir for a star–forming core. Division of the peak  $\text{H}_2$  column density of  $6 \times 10^{21} \text{ cm}^{-2}$  by the filament minor and major axis of the parental core ( $1' \times 5'$  angular size; Figs. 1 and 2, Appendix B2) suggest mean  $\text{H}_2$  densities of  $(0.4\text{--}2.0) \times 10^4 \text{ cm}^{-3}$ . Comparison with model density distributions with central density plateau and  $d \ln(\rho)/d \ln(r) = -2$  for large radii (Fig. 5 of Kauffmann et al. 2008) give a central density  $< 3 \times 10^4 \text{ cm}^{-3}$ . For a source–centered aperture of 4200 AU radius, a mass of only  $(0.14 \pm 0.02) M_\odot$  is derived<sup>1</sup>. Division of this aperture mass by the aperture area gives an aperture–averaged column density of  $\langle N(\text{H}_2) \rangle_{4200 \text{ AU}} = 4.8 \times 10^{21} \text{ cm}^{-2}$ .

These values are unusually low, even for starless cores (Kauffmann et al. 2008). L1148–IRS thus resides in a natal core of unusually low density and column density. In this respect, L1148 is similar to the VeLLO core L1014, which was deemed to be “starless” previous to Spitzer observations. This makes it so interesting.

The mass concentration appears to be centrally peaked: as explained in Appendix B2, cuts through the emission suggest density profiles  $d \ln(\rho)/d \ln(r) \sim -2$ . L1148–IRS actually resides  $7''.6$  (i.e., 2500 AU) offset from the dust emission peak. While this offset is potentially interesting, Kauffmann et al. (2008) use Monte–Carlo experiments to show that this dislocation is only marginally significant given the uncertainties of their data: the beam of  $11''$  size, the low signal–to–noise ratio, possible anomalous refraction, and potential pointing errors of order  $3''$  have to be taken into account. In combination, these effects can lead to apparent offsets

between the VeLLO and dust emission peak position, even if such offsets do not exist.

## 2.2 Spitzer Space Telescope

L1148 was observed by the Spitzer Space Telescope with the Infrared Array Camera (IRAC; AORKEYs 5158144) and the Multi-band Imaging Photometer for Spitzer (MIPS; AORKEY 9440768) as part of the c2d Legacy program (Evans et al. 2003, PID 139). Further Spitzer observations (AORKEYs 14608128, 14615808, 18160384) were acquired by the “cores2deeper” (deep IRAC and MIPS integrations; PID 20386) and “Going Long” (first MIPS 160  $\mu\text{m}$  images of the region; PID 30384) programs. Initial versions of these maps were used in Kauffmann et al. (2005). The images presented here are derived from new mosaics combining all of the aforementioned data. Independent imaging by the Spitzer Gould Belt Legacy Survey (Allen et al., PID 30574) is discussed by Kirk et al. (2009). Spectra of L1148–IRS have been acquired too (PID 30563; AORKEY 18401280), but are not discussed here. Details of the observations, post–processing and source extraction are presented by Evans et al. (2007).

## 2.3 IRAM 30m–telescope

The IRAM 30m–telescope near Granada (Spain) was used to search for an extended outflow from L1148–IRS in the ( $J = 2\text{--}1$ ) transition of  $^{12}\text{CO}$ . Data were taken on 2004 December 19 (single pixel facility receiver; system temperature  $\sim 380 \text{ K}$  in  $T_{\text{mb}}$ –scale, mapped area  $\sim 2' \times 2'$ ) and 2005 July 19 to 21 (HERA multi–beam array;  $\sim 900 \text{ K}$ ,  $\sim 4' \times 4'$ ). The single–pixel maps were already used in Kauffmann et al. (2005). The pointing corrections in azimuth and elevation were below  $3''$ , and the focus corrections below  $0.45 \text{ mm}$ , as checked by regular pointing and focus checks at least once every 3 hours. The intensity scale was converted to the main beam brightness temperature scale according to the efficiencies reported on the IRAM website<sup>2</sup>. Figure 2 gives an overview of the layout of these observations. The data were calibrated and analyzed using IRAM’s CLASS software package<sup>3</sup>.

In parallel to these outflow searches, we used a variety of other tracers to probe the physical and chemical conditions in the dense gas. This includes lines of  $\text{N}_2\text{H}^+$  ( $1\text{--}0$ ) and  $\text{N}_2\text{D}^+$  ( $1\text{--}0$ ), CS ( $2\text{--}1$ ) and ( $3\text{--}2$ ),  $\text{C}^{18}\text{O}$  ( $2\text{--}1$ ),  $\text{HCO}^+$  and  $\text{H}^{13}\text{CO}^+$  ( $1\text{--}0$ ), and HCN ( $1\text{--}0$ ). All observations were obtained in frequency–switched mode using the single–pixel receivers and the autocorrelator backends. The  $\text{N}_2\text{H}^+$  and  $\text{C}^{18}\text{O}$  lines were mapped on 2004 December 19 in the same  $\sim 2' \times 2'$  field for which  $^{12}\text{CO}$  data were obtained. Our  $\text{N}_2\text{H}^+$  and  $\text{C}^{18}\text{O}$  maps were already used in Kauffmann et al. (2005). The remaining lines were observed on 2005 July 19 to 21 in relatively deep integrations towards the three positions near L1148–IRS sketched in Figure 2 (chosen to probe L1148–IRS, its immediate environment, and the neighboring dust core). Focus and pointing uncertainties are as previously quoted for the outflow search. More details are given in Table B1. CLASS was used to calibrate and exploit the data. We removed low–order baselines and partially used Fourier (FFT) filtering to further improve the baseline quality.

<sup>1</sup> The aperture radius of 4200 AU was defined by Motte & André (2001). In Taurus, this size conveniently corresponds to a radius of  $30''$ . Also, Motte & André argue that this radius roughly contains the mass that can be accreted in about  $10^5 \text{ yr}$  of free–fall collapse of an initially hydrostatic sphere of  $\sim 0.2 \text{ km s}^{-1}$  sound speed. However, except for these general considerations, the radius is somewhat arbitrary. We adopt this size to compare with previous observations.

<sup>2</sup> <http://www.iram.es/IRAMES/>

<sup>3</sup> <http://www.iram.fr/IRAMFR/GILDAS/>



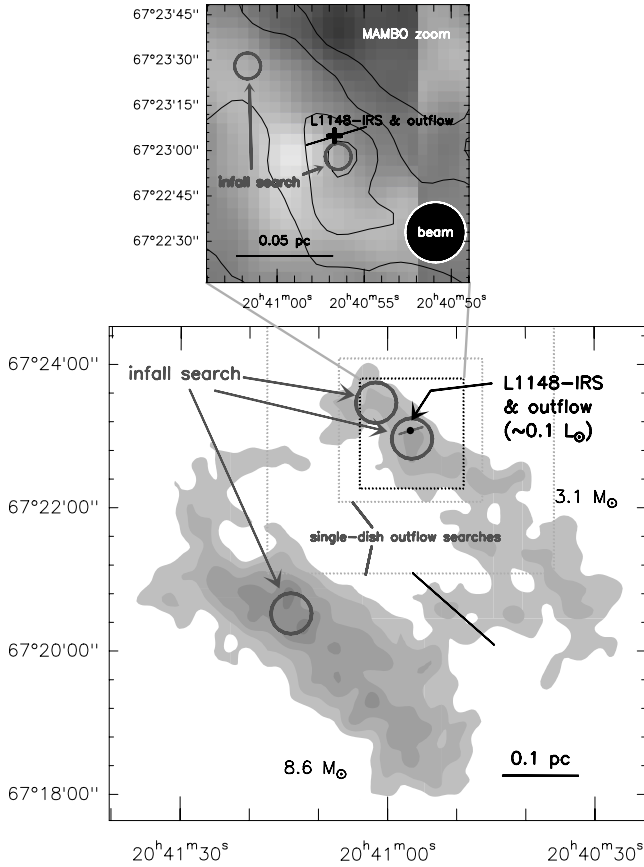


**Figure 2.** Overview of observing strategy and results. As shown by the grey shading in the bottom main panel, the region contains two parallel filaments detected in dust continuum emission. They have masses of  $8.6 M_{\odot}$  and  $3.1 M_{\odot}$ , respectively (a black solid line marks the adopted boundary between the filaments). The position of L1148-IRS and its outflow are indicated by dots and lines, respectively. Boxes centered on L1148-IRS indicate the regions searched for outflows. Circles mark positions probed for dense core contraction motions (Section 2.1, Appendix B5). The top zoom panel presents details of the MAMBO dust emission map in greyscale and contours (starting at, and spaced by,  $2 \text{ mJy per } 11''$  beam after smoothing to the  $20''$  beam marked by a circle). Markers indicate the position of L1148-IRS, its outflow, and of two of the positions searched for contraction motions. Note that L1148-IRS is offset from the nearby dust emission peak (by a marginally significant amount). Coordinates are given for J2000.

## 2.4 KPNO 4m-telescope

As part of a larger program to survey the c2d cores in the near-infrared, deep  $J$ ,  $H$ , and  $K_s$  observations of L1148 were obtained during September of 2004 using FLAMINGOS (Florida Multi-object Imaging Near-IR Grism Observational Spectrometer; Elston 1998) on the 4m-telescope at Kitt Peak National Observatory (KPNO). We use the data acquisition and reduction strategies that have been described in Huard et al. (2006).

## 2.5 Plateau de Bure Interferometer

The Plateau de Bure Interferometer (PdBI) observed L1148-IRS on 6 occasions during the summer of 2006 (project P057; observed on May 13, June 5 and 15, July 22, August 2, and September 1). Between 4 and 5 antennas of the array were used in the ‘D’ configuration (i.e., the most compact one). The 3 mm and 1 mm band receivers were tuned to the ( $J = 1-0$ ) and ( $2-1$ ) transitions

of  $^{12}\text{CO}$ , respectively (115.271202 GHz and 230.538000 GHz; Winnewisser et al. 1997). All 8 units of the correlator took data; for each receiver, 2 units were centered on the line to acquire spectra at  $0.1 \text{ km s}^{-1}$  and  $0.2 \text{ km s}^{-1}$  resolution, and 2 further units were symmetrically displaced from the line to collect continuum data with a bandwidth of 320 MHz. The primary beam sizes were  $20''$  and  $40''$ . The minimum projected baseline in D configuration is  $\sim 20 \text{ m}$ , and so structures larger  $\sim 16''$ , respectively  $\sim 33''$ , are not at all probed by the maps. L1148-IRS was in the phase center of the array.

3C454.3 was typically used for bandpass calibration, while 1928+738 and 2037+511 served as phase calibrators. As usual for the PdBI, MWC349 data yielded the initial flux calibration (assumed to have flux densities of  $1.12 \text{ Jy}$  and  $1.7 \text{ Jy}$  in the 3 mm and 1 mm bands, respectively). Based on this, the fluxes of the other calibrators were fixed and iterated to obtain an optimum calibration across all epochs. The flux calibration can be checked by imaging the phase calibrator 2037+511 in those epochs where it is not used to derive this calibration (i.e., is not held ‘fixed’ in the calibration routines). We find that the observations reproduce the epoch-averaged mean flux density with maximum deviations of 7% and 20% in the 3 mm and 1 mm band, respectively.

The data were calibrated and imaged (including cleaning) using the GILDAS software suite. Here, we use all epochs to construct maps in the 3 mm band, but only the best 4 periods (i.e., excluding July 22 and August 2) are taken in the 1 mm band. This yields beam sizes of  $4''.5 \times 3''.4$  (position angle east of north of  $82^\circ$ ) and  $2''.5 \times 1''.7$  (p.a. of  $65^\circ$ ) at 3 mm and 1 mm wavelength, respectively. To improve the signal-to-noise ratio, the spectra are sampled into bins of  $0.3 \text{ km s}^{-1}$  width. The continuum data are clipped in the spectral range to exclude CO emission from our target source. This yields noise levels in the 3 mm and 1 mm band spectral line data of  $23 \text{ mJy beam}^{-1}$  and  $46 \text{ mJy beam}^{-1}$ , respectively, while we find  $0.39 \text{ mJy beam}^{-1}$  and  $1.0 \text{ mJy beam}^{-1}$  for the continuum data.

## 3 AN OUTFLOW FROM L1148-IRS

Previous analysis failed to establish that L1148-IRS (i) is a YSO and (ii) is physically associated with the L1148 region. Here, we show that the source drives a weak small-scale CO outflow ( $\lesssim 5''$ , about 1800 AU in projection). This confirms the hypotheses (i) and (ii).

### 3.1 A Compact CO Outflow

#### 3.1.1 Single-dish Observations

We initially used the IRAM 30m-telescope to search for an outflow in the  $^{12}\text{CO}$  ( $2-1$ ) line. This search failed (Kauffmann et al. 2005). It is briefly summarized below.

The single-pixel facility receiver was used to map an area of  $2' \times 2'$  size with  $30''$  spacing in frequency-switched mode (layout indicated in Figure 2). The top panels of Figure 3 show an example spectrum from this search: emission from the dense core (as well as ‘telluric’ emission<sup>4</sup> from Earth’s atmosphere) are detected, but

<sup>4</sup> The LSR velocity of the telescope can, e.g., be found from the calculator provided on the homepage of the *Far Ultraviolet Spectroscopic Explorer* (switched to topocentric coordinates), <http://fuse.pha.jhu.edu/support/tools/vlsr.html>,

no obvious outflow signal was found (neither in the form of line wings, nor in terms of clear spatial trends in emission). However, Fourier components, as well as baselines of 2<sup>nd</sup> order, had to be removed during data reduction. Thus, these observations were not sensitive to outflows manifesting in wide and faint emission lines.

Therefore, we later raster-mapped a field of about  $4' \times 4'$  size with  $24''$  spacing using the HERA multi-beam array in position-switched mode (indicated in Figure 2). These data have very flat baselines. Unfortunately, the reference position was not free of emission. Therefore, the data are severely contaminated within about  $\pm 2 \text{ km s}^{-1}$  from systemic velocity. After smoothing to  $0.5 \text{ km s}^{-1}$  velocity resolution, these spectra have a noise level of  $0.8 \text{ Jy beam}^{-1}$  in the main beam brightness scale. Still, no outflow emission was found. Also the mean spectrum averaged over all map pixels does not reveal any CO emission beyond  $\pm 2 \text{ km s}^{-1}$  velocity offset (at a noise level of  $54 \text{ mJy beam}^{-1}$ ).

Figure 3 compares the single-dish observations with the interferometer-detected outflow described below. For this comparison, the PdBI spectra in the  $^{12}\text{CO}$  (2–1) and (1–0) transitions are integrated over source-centered apertures of  $3''$  and  $10''$  radius, respectively. The data show that the single-dish observations are sensitive enough to detect the outflow. The outflow emission is, however, massively confused with the dense core emission. This is similar to the situation in L1014 (Bourke et al. 2005).

### 3.1.2 Interferometric Observations

The non-detection with single-dish telescopes did not rule out the existence of a compact outflow from L1148-IRS, such as the one seen in L1014 (Bourke et al. 2005). We therefore also used IRAM’s Plateau de Bure Interferometer (PdBI) to observe the (1–0) and (2–1) transitions of  $^{12}\text{CO}$ . These observations reveal an outflow from L1148-IRS. As we detail below, it manifests in two symmetric velocity components (Figures 3 and 5) that form a bipolar outflow system (Figure 4).

In the PdBI-derived data cubes, significant  $^{12}\text{CO}$  emission is detected in the  $1.2$  to  $4.2 \text{ km s}^{-1}$  velocity range. (“Significant” means that, in a given position–position–velocity cell, the emission of both  $^{12}\text{CO}$  transitions exceeds the noise level by a factor  $\geq 4$ . The velocity channels are spaced by  $0.3 \text{ km s}^{-1}$ .) The  $\text{N}_2\text{H}^+$ -derived systemic velocity is  $2.60 \text{ km s}^{-1}$  (Section 2.1, Appendix B3). Relative to this we obtain maximum projected velocity offsets of  $-1.4$  to  $+1.6 \text{ km s}^{-1}$  for the  $^{12}\text{CO}$  outflow emission. We approximate this as  $\pm 1.5 \text{ km s}^{-1}$  in the following. Correspondingly, we use velocity ranges of  $0.9$  to  $2.4 \text{ km s}^{-1}$  (blue-shifted lobe) and  $3.0$  to  $4.5 \text{ km s}^{-1}$  (red-shifted lobe; we exclude the central channel at  $2.7 \text{ km s}^{-1}$  for clarity) to calculate the velocity-integrated emission of the lobes.

Figure 4 presents integrated intensities in order to explore the structure of the lobes. These are more apparent in the  $^{12}\text{CO}$  (1–0) data. In this line, the blue-shifted lobe is shorter than the red-shifted one. The extent of the latter lobe is  $5''.5 \pm 0''.3$ , or  $(1800 \pm 100) \text{ AU}$  in projection; to measure this, we find the most elongated contour (at a signal-to-noise level of  $9.5 \pm 1.0$ ), drop to 50% of this intensity, measure this contour’s maximum offset from L1148-IRS, and subtract the beam radius linearly. Manual

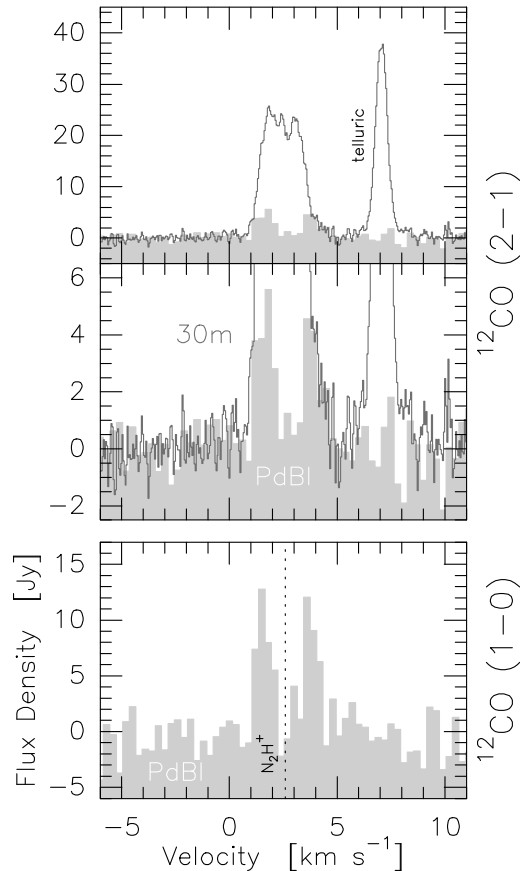


**Figure 3.** CO spectra towards L1148-IRS. The panels show  $^{12}\text{CO}$  ( $J = 2-1$ ) data (top) and ( $J = 1-0$ ) spectra (bottom). For the (2–1) transition, the solid line presents the frequency-switched IRAM 30m-telescope spectrum ( $11''$  beam) taken towards L1148-IRS. The signal near  $7 \text{ km s}^{-1}$  velocity is of telluric origin and thus not relevant here. The shaded histograms portray the data acquired with the Plateau de Bure Interferometer. These spectra are averaged over source-centered apertures of  $3''$  and  $10''$  radius for the (2–1) and (1–0) lines, respectively. The systemic velocity derived from  $\text{N}_2\text{H}^+$  observations (Section 2.1, Appendix B3) is marked by a dashed line.

fitting of the bright and elongated outflow emission with a straight line (Figure 4) gives a most likely position angle of  $107^\circ \pm 22^\circ$ . (To calculate the uncertainty, we derive the position angles when displacing the fitted line by half a beam at  $5''.5$  offset from L1148-IRS.) This fit is guided by the fact that L1148-IRS resides right between the respective intensity peaks of the two lobes; this suggests an outflow direction similar to the position angle of the line connecting the peaks. Unfortunately, though, the emission farther away from the star ( $\gtrsim 5''$ ) shows no clear structure. This leaves the option of a wide-angle outflow propagating in a direction significantly different from the one obtained above.

Figure 3 shows spectra of the outflow emission. Gaussian fits to the spectra, and comparison to the  $\text{N}_2\text{H}^+$  systemic velocity, yield projected velocity offsets of  $-1.0$  and  $+1.2 \text{ km s}^{-1}$  for the  $^{12}\text{CO}$  (1–0) line, respectively  $-0.9$  and  $+1.2 \text{ km s}^{-1}$  for the (2–1) line. We approximate this as  $\pm 1.0 \text{ km s}^{-1}$  in the following. Gaussian line fitting of the PdBI spectra gives velocity-integrated flux densities of  $21.0 \text{ Jy km s}^{-1}$  and  $8.9 \text{ Jy km s}^{-1}$  (15% of the single-dish flux density) for the (1–0) and (2–1) lines, respectively.

The position–velocity diagrams presented in Figure 5 show that the lobes are kinematically well-separated along the entire outflow axis. Some faint outflow features can possibly be traced to

and using the “source” command within the ASTRO program of the GILDAS software package (<http://www.iram.fr/IRAMFR/GILDAS/>). The LSR velocity of telluric lines is the negative of the telescope’s LSR velocity.

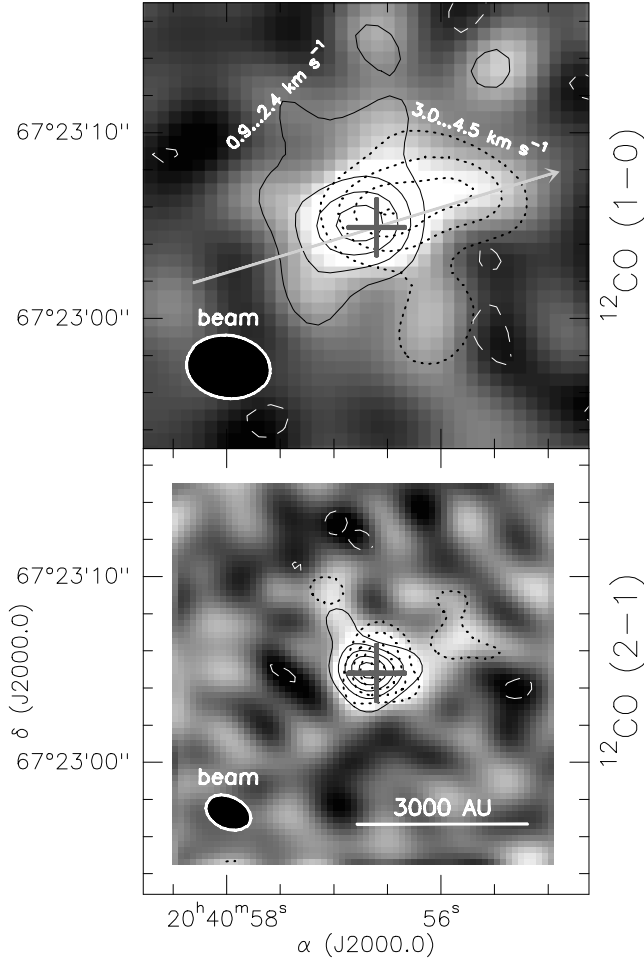


**Figure 4.** The outflow lobes for both  $^{12}\text{CO}$  transitions. The greyscale map presents the emission integrated over the  $0.9$  to  $4.5\text{ km s}^{-1}$  velocity interval. Solid contours outline the emission of the blue-shifted lobe at  $0.9$  to  $2.4\text{ km s}^{-1}$  velocity, while dotted contours delineate the red-shifted lobe at  $3.0$  to  $4.5\text{ km s}^{-1}$ . These contours start at, and are spaced by, the noise level times a factor  $\pm 3$ ; they are dashed for areas with negative emission. The central cross marks the position of L1148-IRS. Ellipses give the beam sizes at half sensitivity. The arrow marks the location and orientation of the position-velocity cut presented in Figure 5.

velocity offsets as large as  $\pm 2.5\text{ km s}^{-1}$ . The  $^{12}\text{CO}$  (2–1) panel reveals that the knot at  $+5''$  offset is detected in several velocity channels, and is therefore probably real. The elongated lobe seen in the (1–0) maps appears to form a counterpart of this knot.

The CO emission cannot come from a circumstellar disk. Keplerian motion at  $1\text{ km s}^{-1}$  speed and  $1800\text{ AU}$  radius would require a central mass of  $2\text{ }M_{\odot}$ . This significantly exceeds the estimated mass of the central star (Section 6.1) and of the dense core material immediately surrounding the YSO (Section 2.1). The emission must thus come from an outflow.

There is a remote chance that the compact CO emission is not from an outflow, but is just an artifact of the interferometer-induced spatial filtering of the dense core emission. We cannot rule this option out. However, as we will show in Section 3.5, the close association of CO emission and L1148-IRS alone is sufficient to reliably demonstrate the protostellar nature of L1148-IRS.

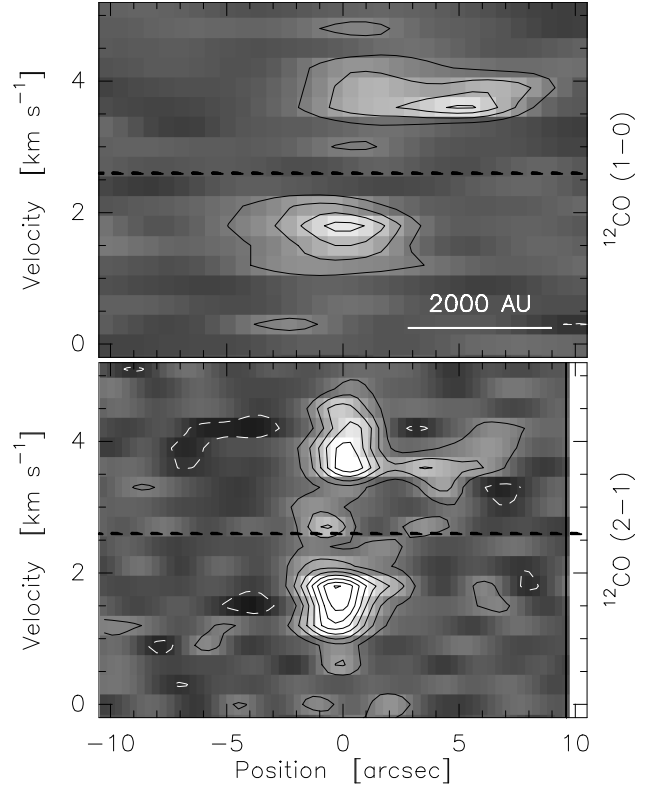


**Figure 5.** Position-velocity diagrams along the trajectory indicated in Figure 4. The spatial origin coincides with L1148-IRS, and the offset increases in the direction of the arrow drawn in Figure 4. Contours start at, and are spaced by, the noise level times a factor  $\pm 2$ . Dashed lines are drawn for negative signal, and solid contours are used otherwise. The horizontal dashed line marks the systemic velocity derived from  $\text{N}_2\text{H}^+$  observations (Section 2.1, Appendix B3).

### 3.2 Outflow Mass and Kinematics

To derive the outflow mass, we assume the  $^{12}\text{CO}$  emission to be optically thin, adopt an  $\text{H}_2$ -to- $^{12}\text{CO}$  abundance ratio of  $10^4$ , a mean mass per  $\text{H}_2$  molecule of  $2.4\text{ H-masses}$ , and use Eq. (A4) of Bourke et al. (1997) to calculate the column densities (for  $^{12}\text{CO}$ , we use a permanent dipole moment of  $0.11\text{ D}$  and a rotational constant of  $57.636\text{ GHz}$ ). We adopt an excitation temperature of  $20\text{ K}$ . This is a bit more than canonical dense core temperatures  $\sim 10\text{ K}$ , but less than the few  $10^2\text{ K}$  observed in outflows of much higher velocity (see, e.g., Santiago-García et al. 2009 for a summary). This temperature uncertainty introduces a moderate mass uncertainty: temperatures in the range  $10$  to  $50\text{ K}$  would give masses different by less than a factor 2. We obtain outflow mass estimates,  $m_{\text{out}}$ , of  $1.3 \times 10^{-3}\text{ }M_{\odot}$  and  $3.9 \times 10^{-4}\text{ }M_{\odot}$  for the  $^{12}\text{CO}$  (1–0) and (2–1) observations, respectively. Correction for typical  $^{12}\text{CO}$  outflow optical depths of 2 to 5 (Levreault 1988) would increase the masses by similar factors. For the (2–1) line, comparison with single-dish data implies a total flux loss of a factor 7 (Figure 3). This could lead to underestimation of the outflow mass by similar factors.

We adopt a characteristic outflow velocity of  $v_{\text{out}} = |\pm 1\text{ km s}^{-1}|$ , and a radial size of  $r = 1800\text{ AU}$ . These are, of course, projected properties, which in principle must be corrected for the inclination angle. This angle is, unfortunately, not known, which introduces systematic uncertainties into our analysis. Using the formalism of Cabrit & Bertout (1990) and Bourke et al. (1997), we derive the properties listed in Table 1. The quoted uncertain-

**Table 1.** Outflow properties. The quoted uncertainties refer to the range in outflow masses derived from the different  $^{12}\text{CO}$  transitions.

Property	Definition	Value
size (radius)	$\frac{r}{\text{AU}}$	1800
velocity	$\frac{v_{\text{out}}}{\text{km s}^{-1}}$	$ \pm 1 $
mass	$\frac{m_{\text{out}}}{10^{-3} M_{\odot}}$	0.4 to 1.3
momentum	$\frac{m_{\text{out}} \cdot v_{\text{out}}}{10^{-3} M_{\odot} \text{ km s}^{-1}}$	0.4 to 1.3
energy	$\frac{m_{\text{out}} \cdot v_{\text{out}}^2 / 2}{10^{-4} M_{\odot} \text{ km}^2 \text{ s}^{-2}}$	0.2 to 0.6
mechanical luminosity	$\frac{m_{\text{out}} \cdot v_{\text{out}}^3 / [2r]}{10^{-5} L_{\odot}}$	0.4 to 1.3
force	$\frac{m_{\text{out}} \cdot v_{\text{out}}^2 / r}{10^{-7} M_{\odot} \text{ km s}^{-1} \text{ yr}^{-1}}$	0.5 to 1.5
dynamical age	$\frac{r / v_{\text{out}}}{10^3 \text{ yr}}$	8.5
rate	$\frac{m_{\text{out}} \cdot v_{\text{out}} / r}{10^{-7} M_{\odot} \text{ yr}^{-1}}$	0.5 to 1.5

ties refer to the range in outflow masses derived from the different  $^{12}\text{CO}$  transitions. Given their linear dependence on  $m_{\text{out}}$ , the outflow properties also suffer from the systematic uncertainties affecting mass estimates.

The properties of L1148-IRS and its outflow are unusual, but not extreme for an embedded YSO. L1148-IRS is less luminous than any source in the comprehensive Wu et al. (2004) outflow compilation. It also has an outflow mass, mechanical luminosity, and force smaller than observed for all (but 4, allowing for uncertainties) of the 292 outflow systems with known luminosity in the Wu et al. study. These trends do not merely reflect the low luminosity of L1148-IRS; for L1148-IRS, the above properties are still 1 to 2 magnitudes below what is derived when extrapolating typical outflow properties from Wu et al. (2004) to the internal luminosity of L1148-IRS. These deviations are, however, marginally within the scatter observed for other YSOs, and the L1148-IRS outflow is thus not extreme. The outflow survey of embedded YSOs by Bontemps et al. (1996) can be used for another comparison. Based on this study, the force of the L1148-IRS outflow is consistent with what is expected for class I sources of comparable internal luminosity. The YSO envelope mass of L1148-IRS does, however, exceed the typical one expected for the observed outflow force by a factor  $\sim 10$ .

André et al. (1999, IRAM04191), Bourke et al. (2005, L1014-IRS) and Phan-Bao et al. (2008, ISO-Oph 102) report outflow properties for other VeLLOs and brown dwarfs. The outflow of L1148-IRS is similar to those of L1014-IRS and ISO-Oph 102 in terms of velocity (all have  $\sim 1 \text{ km s}^{-1}$ ), but its mass ( $\sim 10^{-3} M_{\odot}$  vs.  $\sim 10^{-5} M_{\odot}$ , without mass corrections) and size (1800 AU vs.  $\leq 1000$  AU) appear to be larger. This is small, though, compared to the  $\sim 10 \text{ km s}^{-1}$  velocity range and  $\sim 15000$  AU extent of IRAM04191.

### 3.3 Absence of Compact Dust Emission

Compact dust emission, such as emitted by circumstellar disks, is not detected towards L1148-IRS. At 1 mm and 3 mm wavelength, we observe intensities of  $0.23 \text{ mJy beam}^{-1}$  and  $0.56 \text{ mJy beam}^{-1}$ , respectively. This is insignificant compared to the noise levels reported in Section 2.5. If we add the noise level times a factor 3, we obtain upper flux density limits of  $< 3.2 \text{ mJy}$  and  $< 1.7 \text{ mJy}$ , where we assume that the dust emission should be more compact than the beam.

These upper limits are in line with, e.g., interferometric continuum observations of L1014-IRS (Bourke et al. 2005). To derive mass limits from these flux densities, we adopt the framework laid out by Kauffmann et al. (2008). Assuming dust with temperatures  $\geq 10 \text{ K}$ , this yields mass limits  $< 0.02 M_{\odot}$  and  $< 0.13 M_{\odot}$ , respectively.

### 3.4 Near-Infrared Nebulosity

The near-infrared (NIR) FLAMINGOS imaging observations presented in Figure 6 reveal elongated nebulosity towards L1148-IRS. This nebulosity is likely related to outflows from the star.

L1148-IRS is detected in all bands, but we only use the two bands with the best data (i.e.,  $H$  and  $K_s$ ) for our analysis. Fits of elongated Gaussians to the  $H$ -band image (which has the higher SNR) give a position angle (east of north) of  $133^\circ$  for the major axis. Along this axis,  $H$ -band emission from L1148-IRS above 10% of the peak intensity has a width of  $4''.1$  ( $3''.7$  in the  $K_s$  band), while nearby stars in the image have a width of only  $2''.5$  ( $2''.7$  for the  $K_s$  band) for this position angle. Repetition of this procedure for the minor axis, and removal of the instrument-induced source width at 10% peak intensity, suggests an intrinsic extension of order  $3''.2 \times 2''.4$  or  $1040 \times 780 \text{ AU}^2$ . Both bands reveal an arc-like feature about  $5''$  to the west of L1148-IRS. This could be related to the aforementioned western blob in the red-shifted  $^{12}\text{CO}$  (2–1) outflow lobe.

The CO-detected lobes and the NIR nebulosity are well aligned ( $133^\circ$  vs.  $107^\circ \pm 22^\circ$ ). The nebulosity thus seems to trace structures such as an outflow-blown cavity.

### 3.5 L1148-IRS as a Confirmed VeLLO

As pointed out by Dunham et al. (2008), confirmation of a VeLLO candidate requires (i) that the internal luminosity is below  $0.1 L_{\odot}$ , and (ii) proof of embeddedness in a dense core. In the characterization framework of Dunham et al. (2008), the outflow discovery furnishes the latter. Following the terminology of Dunham et al., L1148-IRS is thus a “confirmed embedded low-luminosity protostar” (their ‘group 1’).

However, given the relatively weak emission, low velocity, and small lobe separation in L1148-IRS, one may doubt that the compact CO emission is really coming from an outflow. As we show here, though, the proximity of compact CO emission and IR source independently demonstrates that L1148-IRS is physically associated to the dense core. Then, L1148-IRS must still be deeply embedded, since there is no other way to produce the Spitzer MIPS emission at the observed intensities (Section 4).

We establish the association by computing the chance alignment probability between background sources (i.e., galaxies) and the  $^{12}\text{CO}$  emission. A background source density  $\sim 2000 \text{ sr}^{-1}$  is to be expected for  $24 \mu\text{m}$  sources brighter  $70 \text{ mJy}$  (Papovich et al. 2004). L1148-IRS and the  $^{12}\text{CO}$  (2–1) emission peaks are aligned



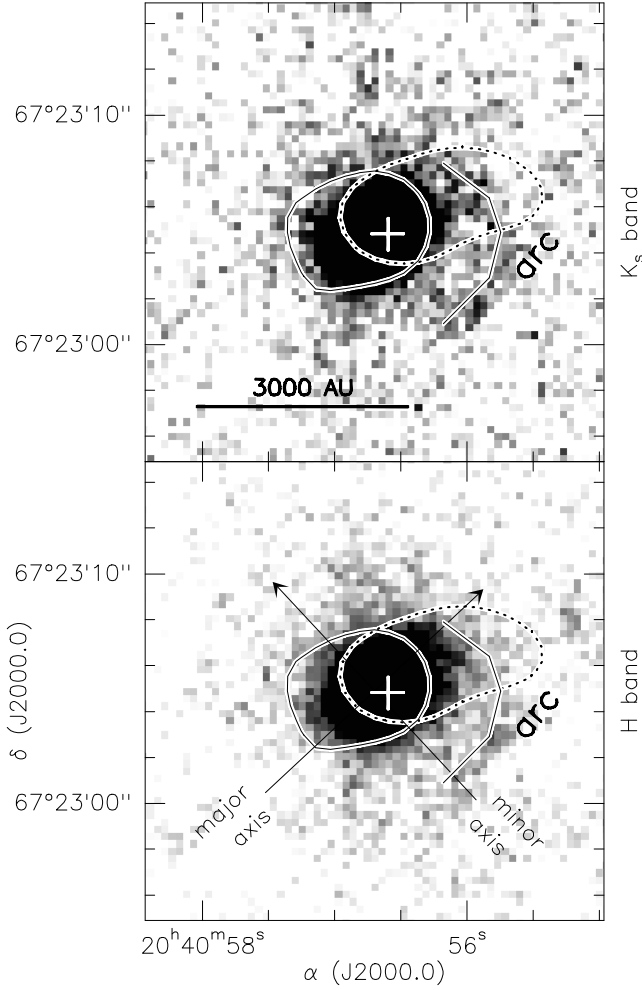


**Figure 6.** Images of L1148-IRS in the  $H$  (bottom panel) and  $K_s$  bands (top panel) as seen by FLAMINGOS, shown as their negative. Contours delineate the  $^{12}\text{CO}$  (1–0) outflow lobes for signals exceeding the noise by a factor 6 (see Figure 4). The arrows indicate positions and directions of the cuts through the intensity distribution that are discussed in the text. The images reveal that L1148-IRS is elongated, with the major axis at position angle  $\approx 133^\circ$ . In addition there is an arc-like extended feature about  $5''$  to the west of L1148-IRS. To facilitate comparison between both images, the arc is indicated by a solid tracer line.

to within  $1''$  distance (Figure 4). For an individual cloud, the probability for chance alignment is thus  $\pi (1'')^2 \cdot 2000 \text{ sr}^{-1} = 1.5 \times 10^{-8}$ . For the entire c2d MAMBO survey, with  $\sim 110$  dust emission peaks, the probability of one chance alignment is  $1.6 \times 10^{-6}$  (assuming that every dust emission peak contains interferometer-detected CO structures like those presented here). There is no realistic option that dense core and L1148-IRS are not physically associated.

#### 4 THE SPECTRAL ENERGY DISTRIBUTION OF L1148-IRS

The outflow observations establish the protostellar nature of L1148-IRS. However, we still need to characterize the embedded infrared source. Here, we gather photometry of this object, sketch a model for the analysis of the observations, and discuss the properties derived using this model.

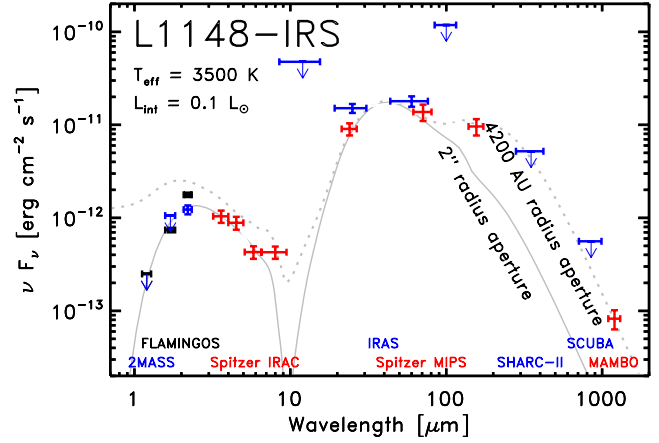


**Figure 7.** The spectral energy distribution of L1148-IRS. Bars represent flux density measurements with their associated uncertainty and filter width, while arrows indicate upper limits. Solid and dashed lines describe a dense core model containing a point source with  $0.1 L_\odot$  internal luminosity and  $3500 \text{ K}$  effective temperature; the solid line holds for an aperture of  $2''$  radius, which is used to model the observations at  $\leq 10 \mu\text{m}$  wavelength, while the dashed line refers to an aperture of  $4200 \text{ AU}$  radius, as applied to the observations at larger wavelengths. This is detailed in Section 4.2.

#### 4.1 Observations

Figure 7 presents the spectral energy distribution (SED) of L1148-IRS. These data are assembled from the 2MASS point source catalogue (Skrutskie et al. 2006), our FLAMINGOS observations, the IRAS faint source catalogue (Moshir & al. 1990), the final release of the c2d source catalogue (Evans et al. 2007), our cores2deeper Spitzer project (PID 20386), our deep MIPS  $160 \mu\text{m}$  survey of cores (PID 30384), SHARC-II imaging by Wu et al. (2007), the SCUBA legacy source catalogue (Francesco et al. 2008), and our c2d MAMBO survey (Kauffmann et al. 2008). Appendix A discusses how we consolidate these data from different origins. Table A1 lists the flux densities in detail.

Integration of the SED yields bolometric luminosities and temperatures of  $0.12 L_\odot$  and  $110 \text{ K}$ , respectively. We derive these parameters using power-laws to interpolate between the detected flux densities. We further assume flux densities scaling with wavelength as  $\lambda^4$  for  $\lambda > 350 \mu\text{m}$  (Kauffmann et al. 2008). Propagation of the flux-weighted observational uncertainties gives uncertainties  $< 20\%$  in luminosity, and  $\pm 15 \text{ K}$  in temperature. This is in agreement with the L1148-IRS characterization by Kauffmann et al. (2005, 2008), but a bit warmer and fainter than what is found by Kirk et al. (2009; probably because they use MAMBO fluxes for larger apertures).

#### 4.2 Modeling

We model the SED of L1148-IRS as a spherical dense core that contains a point source and is externally illuminated by the interstellar radiation field (ISRF). The point source is assumed to emit like a black body of luminosity  $L_{\text{int}}$  and temperature  $T_{\text{eff}}$ ; we refer to these as the internal luminosity and the stellar effective temperature. The ISRF is taken from P  rault (1987). We reduce its intensity at the core surface by a factor 4. This reflects shielding by extended material of a total (surface to surface) extinction of 3 mag, and is necessary to simultaneously match the MAMBO and MIPS3 observations. We adopt dust opacities as Weingartner & Draine (2001) predict for their “case B” and a total-to-selective extinction ratio



of  $R_V = 5.5$  (since this model provides a good fit to observed dust opacities at wavelengths  $\lesssim 10 \mu\text{m}$ ; e.g., Indebetouw et al. 2005). Model flux densities are calculated using a code kindly provided by E. Krügel (e.g., Appendix A of Pillai et al. 2006).

The dense core’s density profile,  $\rho(r)$ , is modeled as a continuous step-wise power law. We truncate the sphere at an outer radius of  $32500 \text{ AU} \approx 0.16 \text{ pc}$ , corresponding to  $\approx 100''$ . The density is assumed to be negligible within the inner truncation radius,  $r_{\text{in}}$ . For most radii, the slope of the density profile is set to  $d \ln(\rho)/d \ln(r) = -2$ . However, good matches of the SED require a flatter density law in some inner part of the sphere. We do this by introducing a constant density between the inner and outer transition radii,  $r_{\text{trans}}^{\text{in}}$  and  $r_{\text{trans}}^{\text{out}}$ . Our fits use  $r_{\text{trans}}^{\text{out}} = 2 \times 10^{14} \text{ m} \approx 1340 \text{ AU}$  (i.e.,  $8''.25$  diameter), since this is large enough to provide good SED fits (as demonstrated by the results below) but is compact enough to be consistent with the steep dust emission intensity profile that rules out extended regions of constant density (Section 2.1). With these assumptions, the density profile is fully defined once the density at the outer truncation radius,  $\rho_{\text{out}}$ , is specified. We fix the latter by requiring the model to exactly match the MAMBO flux density measurement. This eventually leaves two envelope parameters (i.e.,  $r_{\text{in}}$  and  $r_{\text{trans}}^{\text{in}}$ ) and two source parameters (i.e.,  $L_{\text{int}}$  and  $T_{\text{eff}}$ ) unconstrained.

At wavelengths  $< 10 \mu\text{m}$ , we attempt to minimize the mean squared relative difference between the observed and predicted flux densities (i.e., the difference between model and observation, divided by the observation; this property,  $\chi_{\text{rel}}^2$ , takes the role of the classical  $\chi^2$ ). We do not normalize the differences by the observational flux density uncertainties (as usually done to derive  $\chi^2$ ) because the predicted flux densities do sensitively depend on the adopted geometry (e.g., Whitney et al. 2003). In this situation, the deviations between good models and observed flux densities are not dominated by observational uncertainties. We further require that a valid model does strictly not exceed the  $J$ -band limits. The synthetic observations are calculated for an aperture of  $2''$  radius, and they are corrected for an intensity background determined between  $5''$  and  $10''$  radius. This is used to capture the effect of the background subtraction in the 2MASS, FLAMINGOS, and IRAC observations.

At wavelengths  $> 10 \mu\text{m}$ , we require the model to strictly match the observations within their observational uncertainties (except for all IRAS and the MIPS3 bands, which are too uncertain). This appears appropriate since in this wavelength domain, deviations between good model and observation should be dominated by observational uncertainties. We use an aperture of  $4200 \text{ AU}$  radius to calculate synthetic observations. This is exactly the aperture used in MAMBO observations (Section 2.1). The exact aperture size does not matter for the MIPS1 and MIPS2 bands, since the emission originates (in the model) at radii smaller  $4200 \text{ AU}$ .

The PdBI-derived upper limits for dust continuum emission are not useful for our analysis of the SED of the L1148 core on large spatial scales. Specifically, the interferometer probes radii  $\leq 4''.5$ , i.e.  $\leq 730 \text{ AU}$ , while the analysis above considers scales as large as  $4200 \text{ AU}$ . The PdBI maps are only useful to examine the (absence of) disks around L1148-IR, as done in Sec. 3.3.

### 4.3 Results

Figure 8 presents the smallest mean squared relative deviation found (by varying  $r_{\text{in}}$  and  $r_{\text{trans}}^{\text{in}}$ ) for a given pair of luminosity and temperature. We find a minimum value of 0.08. This corresponds

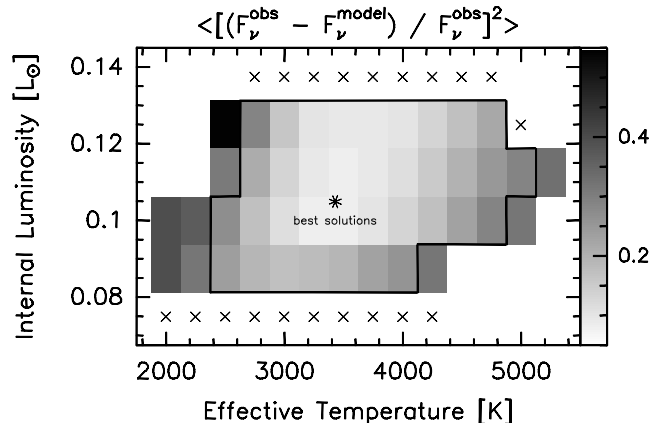


**Figure 8.** Quality of SED fits in dependence on the model effective temperature and internal luminosity. Only cells with shading or crosses have been examined. Grey shading gives  $\chi_{\text{rel}}^2$ , the mean squared relative deviation between SED model and observations at wavelengths  $< 10 \mu\text{m}$ . Crosses are drawn if no model can fit all of the SED constraints. As explained in the main text, only solutions with  $\chi_{\text{rel}}^2 < 0.3$  are deemed acceptable. These solutions are enclosed by a black line. The modeling thus constrains the internal luminosity to  $0.08 \lesssim L_{\text{int}}/L_{\odot} \lesssim 0.13$  and the effective temperature to  $2500 \lesssim T_{\text{eff}}/\text{K} \lesssim 5000$ .

to a mean deviation of  $\sqrt{0.08} = 28\%$  between the observations and the model for wavelengths  $< 10 \mu\text{m}$ . Here, we require that good fits not to exceed this mean deviation by more than a factor 2, i.e., we require  $\chi_{\text{rel}}^2 < 0.30 \approx (2 \times 0.28)^2$ . For certain luminosity–temperature pairs, no solution exists, since no model simultaneously fits the strict  $J$ -band and MIPS constraints.

The modeling constrains the internal luminosity to

$$L_{\text{int}} = 0.08 \text{ to } 0.13 L_{\odot}.$$

L1148-IRS does thus marginally fulfill the VeLLO luminosity criterion of  $L_{\text{int}} \leq 0.1 L_{\odot}$ . The luminosity is well constrained, since it only requires a good SED match and does not sensitively depend on model parameters. This is different for the effective photospheric temperature, which we find to be  $T_{\text{eff}} = 2500$  to  $5000 \text{ K}$ . The temperature basically follows from the SED slopes at wavelengths  $< 10 \mu\text{m}$ . Unfortunately, at these wavelength the spherical geometry of our model is probably too simplistic to capture the relevant inner envelope extinction and scattering processes. This induces further systematic uncertainties. In any event, though, a central source of several  $1000 \text{ K}$  must be present to explain the detections in the 2MASS/FLAMINGOS bands.

The SED of L1148-IRS is thus consistent with the idea of L1148-IRS being embedded in the dense core. In particular, this model provides a quantitative explanation for the failure to detect the VeLLO with SHARC-II. Initially, this lack of bright  $350 \mu\text{m}$  emission was interpreted as evidence against L1148-IRS being an embedded VeLLO, since all other VeLLOs show this emission (Wu et al. 2007; Dunham et al. 2008). Our SED model shows, though, that no emission is to be expected, even if an embedded source is present. Slightly more sensitive  $350 \mu\text{m}$  observations should be able to detect emission, though.

## 5 VELLO NATAL CORES AND OUTFLOWS

Comprehensive understanding of L1148-IRS and other VeLLOs requires a good knowledge of the environment in which these ob-

jects form. Therefore, we launched an investigation of the properties of the L1148 dense core. These results, as well as those for other VeLLOs, are collected here to support our further discussion. We also include additional data on outflows. Sections 5.3 and 5.4 summarize this information.

### 5.1 Data for L1148–IRS

Section 2.1 summarizes the data situation for L1148. The information is collected from Kauffmann et al. (2005) and Kauffmann et al. (2008). As described in this summary, some of the data are also presented in Appendix B. Please refer to those sections for details.

### 5.2 Data for other VeLLOs

Here, we review the properties of known and proposed VeLLOs. First, we assess the quality of VeLLO candidates. Specifically, we consider objects that have previously been discussed to be similar to L1014–IRS, have indications for luminosities  $\leq 0.1 L_{\odot}$ , or were discussed in the context of Brown Dwarf formation.

Visual inspection of Spitzer images of Oph B–11 (Greaves et al. 2003) does not show any far–infrared counterpart. The core may actually be starless and is not considered further here. We also tentatively remove Lupus 3 MMS (Tachihara et al. 2007) and L1415–IRS (Stecklum et al. 2007) from the VeLLO category. In these cases, estimation of the internal luminosity on basis of the flux density at  $70 \mu\text{m}$  wavelength (Dunham et al. 2008) suggests luminosities significantly exceeding the VeLLO limit of  $0.1 L_{\odot}$ . We rate IC1396A: $\gamma_b$  (Reach et al. 2009) as a source of unclear type, since the above luminosity estimate is not possible for this source. Preliminary photometry of the VLA source J025616+192703 in the L1457 dense core implies a low luminosity (Heithausen & Böttner 2010), but data are too limited to judge the probability that this really is a YSO and not a background object. Barrado et al. (2009) present SSTB213 J041757, a possible VeLLO candidate in Taurus. Luhman & Mamajek (2010) show that this is unlikely to be a Taurus YSO, though, and SSTB213 J041757 is thus excluded here.

Chen et al. (2010) and Enoch et al. (2010) have recently presented good candidates for “first hydrostatic cores” (Larson 1969) with internal luminosities  $\lesssim 0.01 L_{\odot}$ . These could be dense cores which have just become optically thick to their own radiation, before eventually collapsing into a more compact YSO. Such objects have a low age and luminosity, and they are embedded in a dense core. This qualifies first hydrostatic cores as VeLLOs. The Chen et al. and Enoch et al. sources will be included in our comparison once their nature has been established by decisive evidence.

Table 2 lists 7 well–studied VeLLOs in order of decreasing aperture mass,  $M_{4200\text{AU}}$ . It evaluates some criteria for dense core evolution forwarded by Crapsi et al. (2005a). By comparing properties like column densities of dense gas tracers to characteristic thresholds, these criteria essentially test whether a dense core contains a significant mass of high density gas. Where appropriate (i.e., not when evaluating the CO depletion factor: Appendix B4), we convert published values to match the dust properties adopted by Kauffmann et al. (2008; their Appendix A). We also list internal luminosities and results of outflow searches, as reported in the respective discovery paper. Distance–normalized flux densities at  $1.8 \text{ cm}$  wavelength, as reported by Scaife et al. (2010), characterize the radio emission properties of the VeLLOs.

### 5.3 Properties of VeLLO Natal Cores

The VeLLOs in Table 2 can roughly be divided into two groups. The first group is composed of L1521F, Cha–MMS1, and IRAM04191. These cores fail in none of the Crapsi et al. (2005a) criteria for “evolved” dense cores (if we stick only to criteria that can be tested with existing data). For instance, these cores are very dense (in terms of volume and column density), they have strongly peaked density profile (as indicated by small values of  $r_{70\%}$ , i.e., the radius of the dust emission contour at 70% peak intensity; Crapsi et al. 2005a), and the inner regions of the dense core are in an advanced stage of chemical evolution (i.e., CO depletion, and production of deuterated  $\text{N}_2\text{H}^+$ ). Crapsi et al. (2005a) argued that their criteria select dense cores relatively close to the onset of protostellar collapse. It is thus not surprising to find that collapse has indeed started in some of these objects.

The second group is composed of “unevolved” dense cores, that fail in at least one of the Crapsi et al. criteria; these cores have relatively low (column) densities, and there are often no signs of advanced chemistry. Following Crapsi et al. (2005a), these dense cores are not expected to collapse and form stars. Section 6.3 explores how stars might still have formed in these cores. The most prominent member of this group is L1014; the discovery of a Spitzer source in this core of low density, which was believed to be “starless”, was a big surprise (Young et al. 2004). Also L1148 belongs to this group.

*The terminology used above is not meant to indicate that “unevolved” cores mature and eventually become “evolved” ones! It is only used to indicate the relation to the Crapsi et al. criteria.*

In summary, some VeLLOs fulfil the Crapsi et al. (2005a) criteria for evolved cores, while others do not. Since star formation is ongoing in all cores listed in Table 2, the initial conditions for stars to form appear to be very diverse.

L1148–IRS different from the other VeLLOs in that this source appears to have the lowest aperture mass of all VeLLOs. It also features the lowest  $\text{N}_2\text{H}^+$  line width ( $[0.232 \pm 0.048] \text{ km s}^{-1}$ ; the next higher value for VeLLOs is  $0.3 \text{ km s}^{-1}$  for L1521F). Finally, L1148 is the only “unevolved” VeLLO core in which inward motions have been detected. Since line asymmetries are easier detected for narrow lines (Eq. B2), this might be a consequence of the low  $\text{N}_2\text{H}^+$  line width.

### 5.4 Properties of VeLLO Outflows

VeLLOs differ vastly in their outflow properties. For example, only 2 out of the 7 VeLLOs discussed in Table 2 (i.e., IRAM04191 and L673–7–IRS) drive a “prominent” extended outflow that can easily be detected using single–dish telescopes. The remaining VeLLOs all appear to drive outflows (based on Spitzer image morphology and interferometer observations), but sensitive high–resolution observations are needed to detect these (like those presented in Section 3).

As seen in Table 2, the presence of prominent outflow activity does not appear to correlate with any other dense core property. In the present sample, to be specific, an extended outflow is driven by a VeLLO in one of the most “evolved” cores, i.e. IRAM04191, which also has a large aperture mass. But also the VeLLO in L673–7 has a prominent outflow, despite a very moderate aperture mass and failure in some of the Crapsi et al. criteria. In addition, cores more evolved than IRAM04191 (e.g., L1521F), as well as cores very similar to L673–7 (e.g., L1014), do not drive such flow. This diversity could be a consequence of VeLLO evolution; VeLLOs

**Table 2.** VeLLOs and their Natal Cores

Property	Evolved Cores			Unevolved Cores			
	L1521F	Cha-MMS1	IRAM04191	L673-7	L1014	L328	L1148
<i>protostar properties:</i>							
outflow	Y	?	Y	Y	Y	?	Y
extended outflow	n	n	Y	Y	n	n	n
$L_{\text{int}}/L_{\odot}$	$\approx 0.04$	$[\approx 0.01]$	$\approx 0.07$	$\approx 0.04$	$\approx 0.09$	$\approx 0.05$	$\approx 0.10$
$F_{1.8\text{cm}} d^2 / 10^{-2} \text{ mJy kpc}^2$	0.3	?	0.3	0.5	1.9	?	$\leq 0.7$
<i>dense core properties:</i>							
$M_{4200} \text{ AU} / M_{\odot}$	0.87	[0.8]	0.60	0.39	0.36	[> 0.13/0.31]	0.14
$\langle N(\text{H}_2) \rangle_{4200 \text{ AU}} / 10^{22} \text{ cm}^{-2}$	3.0	[2.7]	2.0	1.3	1.2	[> 0.4/1.1]	0.5
$N(\text{N}_2\text{D}^+) > 1.0 \times 10^{12} \text{ cm}^{-2}$	Y	[Y]	?	?	n	n	n
$N(\text{N}_2\text{H}^+) > 8.5 \times 10^{12} \text{ cm}^{-2}$	Y	[Y]	Y	?	n	Y	n
$N(\text{N}_2\text{D}^+)/N(\text{N}_2\text{H}^+) \geq 0.1$	Y	Y	?	?	Y	n	?
$f_{\text{d}}(\text{CO}) > 10$	Y	?	?	?	n	n	n
$n_{\text{c}}(\text{H}_2) > 2.5 \times 10^5 \text{ cm}^{-3}$	Y	Y	Y	n	n	n	n
$\Delta v(\text{N}_2\text{H}^+) > 0.25 \text{ km s}^{-1}$	Y	Y	Y	Y	Y	Y	n
inward motions	Y	?	Y	n	n	n	Y
$r_{70\%} < 4800 \text{ AU}$	Y	Y	Y	Y	Y	Y	Y

**References.** Data are from Lee et al. (1999, 2009); André et al. (1999); Motte & André (2001); Belloche et al. (2002, 2006); Young et al. (2004); Crapsi et al. (2005a,b); Bourke et al. (2005, 2006); Dunham et al. (2006, 2010a); Kauffmann et al. (2005, 2008, and this work); and Scaife et al. (2010)

**Notes.** The dense core properties are compared to the criteria for “evolved” cores by Crapsi et al. (2005a) after conversion of the limiting density to our choice of dust emission properties. A ‘Y’ marker indicates that a criterion is met, a ‘n’ marker that it is not, a question mark that the data are insufficient to decide. Properties marked by square brackets ([...]) are not readily available from the relevant publications and must be gleaned from the other published properties. For Cha-MMS1, the  $\text{N}_2\text{H}^+$  and  $\text{N}_2\text{D}^+$  column densities have to be derived from the abundances and dust column densities reported by Belloche et al. (2006). The aperture mass is derived from models for the density structure presented in the same publication. For L328-IRS, the envelope masses are from lower limits of the 1.2 mm wavelength dust emission (Lee et al. 2009; 70 mJy within 2000 AU radius) and integration of the Lee et al. envelope density model to 4200 AU radius. We deviate from the Crapsi et al. practice to infer inward motions from asymmetries in the  $\text{N}_2\text{H}^+$  lines; instead, inward motions are either inferred from the analysis of line shifts (L1521F, L673-7, L1014, L328, and L1148), or from detailed modeling of line shapes (IRAM04191). For all sources the uncertainty in the internal luminosity is of order  $\pm 0.03 L_{\odot}$ .

without outflows might be in a stage preceding or following an accretion phase, in which prominent outflows are produced. It is not clear whether other options — i.e., VeLLO formation without prominent outflows in any evolutionary stage — provide credible models.

It is also not clear how the presence of prominent outflows relates to the concept of “episodic accretion”, i.e., accretion (and thus outflow generation) occurring only during short episodes of the protostellar lifetime (Kenyon et al. 1990). In this picture, VeLLOs would quasi-periodically create and gradually lose their prominent outflows. Dynamical ages for the outflows of IRAM04191 and L673-7-IRS suggest that individual outflow periods<sup>5</sup> last a few  $10^4$  yr in VeLLOs. If VeLLOs without prominent outflows are indeed in a dormant stage, this stage should prevail for an even longer timescale ( $> 10^4$  yr), as indicated by the large fraction of VeLLOs without such outflows. Combination of Spitzer source counts (Evans et al. 2009) with evolutionary models (Dunham et al. 2010b) indeed shows that YSOs might accrete most of their mass in  $\lesssim 10$  bursts occurring over a period  $\sim 2 \times 10^5$  yr. These models do thus imply dormant periods of several  $10^4$  yr, just as suggested by VeLLO outflow statistics.

## 6 DISCUSSION: L1148-IRS IN CONTEXT

### 6.1 Evolutionary Stage & Mass of L1148-IRS

L1148-IRS has a bolometric temperature ( $110 \pm 15$ ) K (Section 4.1). This implies that L1148-IRS belongs to the protostellar class I, and suggests an age  $< 7 \times 10^5$  yr (Evans et al. 2009). We use this limit in the following.

As shown by Young et al. (2004), the internal luminosity of  $\leq 0.1 L_{\odot}$  limits the present mass of all VeLLOs to a most likely value  $\lesssim 0.1 M_{\odot}$ , if the luminosity is dominated by accretion power. This is probably the case for L1148-IRS, since it appears to drive an (supposedly accretion-powered) outflow. Further, the young brown dwarf FU Tau (a class II object of  $\lesssim 10^6$  yr) has a luminosity of  $0.2 L_{\odot}$  (Luhman et al. 2009;  $\geq 0.1 L_{\odot}$  for the brightest component, if FU Tau is an unresolved binary). This object might be unusually luminous (Luhman et al. 2009), but its properties support the notion that YSO luminosities  $\lesssim 0.1 L_{\odot}$  imply a mass in the brown dwarf domain. Thus, we find that the most likely present-day mass is  $\lesssim 0.1 M_{\odot}$ .

Comparison with evolutionary tracks by Baraffe et al. (1998) and Chabrier et al. (2000) suggest a very conservative mass limit  $\ll 0.35 M_{\odot}$  (when reducing the model luminosities by a factor 3; Reiners et al. 2005). Models by Wuchterl & Tscharnuter (2003) suggest  $< 0.1 M_{\odot}$ , if one only considers early stages with significant accretion. Unfortunately, their models are not well tested against observations.

To understand the collapse conditions in L1148, consider the collapse of a hydrostatic isothermal sphere of radius  $R$  that is subject

<sup>5</sup> Prominent outflows are detectable during this period. This does, however, not require that they are continuously driven during this time.



to an environmental pressure,  $P_{\text{env}}$ . To be unstable, the sphere must have a mass

$$M > 2.0 M_{\odot} \left( \frac{T_g}{10 \text{ K}} \right)^2 \left( \frac{R}{0.1 \text{ pc}} \right), \quad (1)$$

and the pressure must obey

$$\frac{P_{\text{ext}}}{k_B} > 3.3 \times 10^4 \text{ cm}^{-3} \left( \frac{T_g}{10 \text{ K}} \right)^4 \left( \frac{R}{0.1 \text{ pc}} \right)^{-2} \quad (2)$$

(Bonnor 1956 and Ebert 1955;  $k_B$  is Boltzmann's constant). Star formation requires that the inner parts of the protostellar envelope are unstable<sup>6</sup>. We can use the aforementioned aperture mass,  $M_{4200\text{AU}}$ , to test this condition. For  $R = 4200 \text{ AU}$  and  $T_g = 10 \text{ K}$ , Eq. (1) yields the condition  $M > 0.41 M_{\odot}$ . Thus,  $M_{4200\text{AU}}$  fails the condition for gravitational instability. The reservoir actively forming the VeLLO must therefore have a radius  $< 4200 \text{ AU}$ . This implies an unstable mass smaller  $M_{4200\text{AU}}$ , i.e.  $< 0.14 M_{\odot}$  (Section 2.1). Radii  $< 4200 \text{ AU}$  also imply a pressure  $P_{\text{ext}}/k_B > 8 \times 10^5 \text{ cm}^{-2}$ . As we discuss in Section 6.3, this pressure is relatively high. This has implications on VeLLO formation models.

Combined with the present-day mass of L1148-IRS,  $< 0.1 M_{\odot}$ , this estimate of the collapsing mass suggests a final mass  $< 0.24 M_{\odot}$ . If this VeLLO has a present-day mass  $< 0.05 M_{\odot}$ , and the immediate envelope of  $< 0.14 M_{\odot}$  is accreted with an efficiency  $\sim 1/3$  (as deemed typical; e.g., Alves et al. 2007), then L1148-IRS could have a final mass even below the brown dwarf limit. After L328-IRS (Lee et al. 2009), this is the second VeLLO for which such a small final mass is derived.

## 6.2 The Nature and Evolution of VeLLOs

There is probably general consent that VeLLOs have a most likely present-day mass  $< 0.1 M_{\odot}$  (Section 6.1). The final mass at the end of the accretion phase might, however, be much larger.

VeLLO natal cores differ significantly in the mass of gas at high density they contain (Section 5). Since VeLLOs form from this gas, these differences may suggest that different VeLLOs take different evolutionary paths (Bourke et al. 2006). Some may have significant future accretion and attain a stellar final mass (André et al. 1999), while lack of accretion in others could render these objects young brown dwarfs (Young et al. 2004; Huard et al. 2006). Table 2 thus presents a first attempt to systematically characterize the likeliness of these different evolutionary paths for several VeLLOs. The number of positive indicators for significant amounts of high density gas near the VeLLO increase towards the left of Table 2. The VeLLO final mass is therefore likely to increase in this direction too. L328-IRS and L1148-IRS hold a peculiar position among VeLLOs, given that their most likely final mass is very low ( $< 0.15 M_{\odot}$  and  $< 0.24 M_{\odot}$ , respectively; see Lee et al. 2009 and Section 6.1).

## 6.3 Formation of Brown Dwarfs: Lessons from L1148

One unsolved aspect of isolated brown dwarf (BD) formation is the large difference between the final BD mass,  $M_{\text{BD}} \lesssim 0.08 M_{\odot}$ , and

the expected mass of the collapsing natal dense core,  $M$ : in most cases  $M \gg M_{\text{BD}}$ . L1148-IRS can be used to study this problem, even in case this VeLLO has a final mass exceeding the BD mass limit.

Consider once again pressure-bound hydrostatic isothermal spheres. Combination of Eqs. (1, 2) yields the condition

$$M > 1.2 M_{\odot} \left( \frac{T_g}{10 \text{ K}} \right)^4 \left( \frac{P_{\text{env}}/k_B}{10^5 \text{ K cm}^{-3}} \right)^{-1/2} \quad (3)$$

for unstable spheres. This system will form a star (or BD) of mass  $M_{\star} = \eta M$ , where  $\eta \leq 1$  is the star formation efficiency. For typical temperatures ( $\approx 10 \text{ K}$ ) and pressures (a few  $10^5 \text{ K cm}^{-3}$ ; e.g. Bertoldi & McKee 1992), one obtains the collapse condition  $M \gtrsim 1 M_{\odot}$ . Typical values of  $\eta$  are believed to be  $\sim 1/3$  (e.g., Alves et al. 2007), yielding typical stellar masses  $\sim 0.3 M_{\odot}$ .

In this framework, to achieve lower stellar masses, BD formation requires unusually small temperature ( $T_g \ll 10 \text{ K}$ ), large pressure ( $P_{\text{env}}/k_B \gg 10^5 \text{ K cm}^{-3}$ ), low efficiency ( $\eta \ll 1/3$ ), or a combination of these. L1148-IRS provides a test case for such reasoning: Eq. (1) suggests  $M < 0.14 M_{\odot}$  for the collapsing core in this region.

The structure of the L1148 core thus appears to require peculiar environmental conditions. We have no satisfying explanation why and in which sense (temperature, pressure, etc.) these should prevail in L1148. One can, however, speculate that the unusual kinematic conditions in this region might have played a role: multiple velocity components (in  $\text{C}^{18}\text{O}$ ), velocity jumps near L1148-IRS (in CCS) and contraction motions on spatial scales  $\gtrsim 0.3 \text{ pc}$  are not commonly observed in dense cores (see Section 2.1 and Appendix B3).

The environmental conditions in L1148 have actually been explored by Nutter et al. (2009). Spatial offsets between intensity peaks at different wavelengths are consistent with external heating of the L1148 core. One could imagine that the core is sculpted by such a radiation field. Kirk et al. (2009) suggests indeed that the entire Cepheus Flare Complex is shaped by external triggering. Related externally triggered compression events would be suited to produce low critical masses via an increase in  $P_{\text{env}}$ .

It might, of course, also be that the initial unstable mass of the dense core was  $\sim 1 M_{\odot}$ , as suggested by Eq. (3), but that we now observe a much more evolved phase, where the initial mass is no longer relevant. Lee et al. (2009), for instance, suggest that L328-IRS might have moved out of its natal core. This would leave this VeLLO with a small mass reservoir to accrete from. Huard et al. (2006) present a similar argument for L1014-IRS. The complex kinematics in L1148 might suggest such a scenario also for L1148-IRS. In fact, Section 2.1 shows that there is a possible — though not significant —  $7''.6$  spatial offset (i.e.,  $2500 \text{ AU}$ ) between L1148-IRS and the core's column density peak. The growth of L1148-IRS might thus be stunted, because it has detached from the dense core from which it cannot accrete from it any longer.

Similarly, L1148-IRS could be in a very advanced stage of evolution where most of the envelope has been dispersed. In principle, strong VeLLO outflows (e.g., as those from IRAM04191; André et al. 1999) might be able to do this.

The credibility of these scenarios is unclear, though. Consider L1148-IRS as an example. Section 6.1 suggests that the present-day mass of this VeLLO is  $\lesssim 0.1 M_{\odot}$ . The immediate environment of L1148-IRS contains  $\sim 0.14 M_{\odot}$  (from the  $4200 \text{ AU}$  aperture mass). If outflows have dispersed the gas, they must thus have disrupted a core of about  $0.75 M_{\odot}$ . It is not known whether dispersal

<sup>6</sup> To be specific, this is a requirement only for models with inside-out collapse. The evolution of these collapsing spheres is similar to those studied by Shu (1977). One major difference, though, is that Shu considers — strictly speaking — infinite spheres with singular density profiles. His structures are unstable to perturbations at all radii, just as required here.



by outflows is efficient enough to do this (Arce et al. 2007). Similarly, it is not obvious how VeLLOs should be able to leave their parental dense core. That would require that accretion from the gas reservoir onto the VeLLO increases the relative velocity between the gas reservoir and the VeLLO. This seems unlikely.

## 7 SUMMARY

We present a detailed analysis of a candidate VeLLO in the Cepheus Flare, L1148-IRS. This work goes beyond the initial announcement of discovery (Kauffmann et al. 2005) by presenting: (i) a comprehensive and sensitive search for a CO outflow; (ii) detailed modelling of the observed spectral energy distribution; and (iii) extensive discussions of the properties of the natal dense core. In addition, (iv) the analysis is augmented by presenting L1148-IRS in the context of an up-to-date VeLLO catalogue. The main conclusions are as follows.

(1) L1148-IRS drives a compact ( $\sim 5''$ , about 1800 AU in projection) CO outflow (Section 3). This confirms L1148-IRS as a clear-cut protostar, and associates it with L1148 through its velocity. The outflow can only be detected in interferometer maps, such as those from the Plateau de Bure Interferometer presented here; single-dish data, e.g. from the IRAM 30m-telescope, do not reveal it. Weak compact ( $\sim 2''$ ) probable outflow nebulosity is seen near  $2\mu\text{m}$  wavelength.

(2) Modelling of the spectral energy distribution suggests the presence of a point source of  $0.08$  to  $0.13 L_{\odot}$  and  $T_{\text{eff}} = 2500$  to  $5000$  K effective photospheric temperature (Section 4). Strong emission near  $100\mu\text{m}$  wavelength requires this source to be deeply embedded in the natal dense core; it corresponds to a source of infrared class 0 or I. L1148-IRS does therefore meet all criteria to be a VeLLO (i.e.,  $L \leq 0.1 L_{\odot}$  and embeddedness in a core), though this is just marginally the case for the luminosity.

(3) The natal dense core is characterized by densities and column densities that are unusually low for a star-forming core (Section 2.1). Multiple velocity components, velocity jumps, and velocity gradients are detected in the core, pointing towards unusual kinematic conditions in this region. Strong evidence for contraction motions is found in asymmetries of optically thick lines.

(4) Among all VeLLOs known, L1148-IRS stands out as the one with the lowest envelope mass and a core of unusually low (column) density (Table 2 in Section 6). It is a riddle how a star could have formed under these conditions.

As in all other VeLLOs, the low luminosity suggests a substellar present mass for L1148-IRS, i.e.  $< 0.1 M_{\odot}$ . The gravitationally unstable mass surrounding L1148-IRS appears to be  $\lesssim 0.14 M_{\odot}$ . Their sum suggests a very low final mass, so that L1148-IRS may be a good candidate for a proto brown dwarf forming in isolation.

## ACKNOWLEDGEMENTS

We are indebted to our local IRAM contacts, Arancha Castro-Carrizo and Frédéric Gueth, who changed their busy schedule to simplify our travel arrangements for a data reduction visit. We thank Endrik Krügel for providing us with a custom-modified dust radiative transfer code. Mike Dunham was so kind to check our VeLLO catalogue (Table 2, Section 5.2) against his notes. JK is deeply indebted to FB, Karl Menten, Malcolm Walmsley, Johannes Schmid-Burgk, and TP. This work would have been impossible

without their continuous and unconditional support. He also thanks Di Li and Paul Goldsmith, his hosts at JPL, for making this research possible. This project was supported by an appointment of JK to the NASA Postdoctoral Program at the Jet Propulsion Laboratory, administered by Oak Ridge Associated Universities through a contract with NASA. His research was executed at the Jet Propulsion Laboratory, California Institute of Technology, under a contract with the National Air and Space Administration. Partial support for TLB was provided by NASA through contracts 1279198 and 1288806 issued by the Jet Propulsion Laboratory, California Institute of Technology, under NASA contract 1407. CWL acknowledges the support by Basic Science Research Program through the National Research Foundation of Korea funded by the Ministry of Education, Science and Technology (2010-0011605).

## REFERENCES

- Alves, J., Lombardi, M., & Lada, C. 2007, *Astron. & Astrophys.*, 462, L17
- André, P., Motte, F., & Bacmann, A. 1999, *Astrophys. J. Letters*, 513, L57
- Andre, P., Ward-Thompson, D., & Barsony, M. 1993, *Astrophys. J.*, 406, 122
- Arce, H. G., Shepherd, D., Gueth, F., Lee, C.-F., Bachiller, R., Rosen, A., & Beuther, H. 2007, *Protostars and Planets V*
- Baraffe, I., Chabrier, G., Allard, F., & Hauschildt, P. 1998, *Astron. & Astrophys.*, 337, 403
- Barrado, D., Morales-Calderón, M., Palau, A., Bayo, A., de Gregorio-Monsalvo, I., Eiroa, C., Huéramo, N., Bouy, H., Morata, O., & Schmidtobreick, L. 2009, *Astronomy and Astrophysics*, 508, 859
- Belloche, A., André, P., Despois, D., & Blinder, S. 2002, *Astron. & Astrophys.*, 393, 927
- Belloche, A., Parise, B., van Der Tak, F., Schilke, P., Leurini, S., Güsten, R., & Nyman, L.-A. 2006, *Astron. & Astrophys.*, 454, L51
- Bertoldi, F., & McKee, C. F. 1992, *The Astrophysical Journal*, 395, 140
- Bonnor, W. 1956, *Monthly Not. Roy. Astron. Soc.*, 116, 351
- Bontemps, S., Andre, P., Terebey, S., & Cabrit, S. 1996, *Astron. & Astrophys.*, 311, 858
- Bourke, T., Crapsi, A., Myers, P., Evans, N., Wilner, D., Huard, T., Jørgensen, J., & Young, C. 2005, *Astrophys. J. Letters*, 633, L129
- Bourke, T., Garay, G., Lehtinen, K., Koehnkamp, I., Launhardt, R., Nyman, L.-A., May, J., Robinson, G., & Hyland, A. 1997, *Astrophys. J.*, 476, 781
- Bourke, T. L., Myers, P. C., Evans II, N. J., Dunham, M. M., Kauffmann, J., Shirley, Y. L., Crapsi, A., Young, C. H., Huard, T. L., Brooke, T. Y., Chapman, N., Cieza, L., Lee, C. W., Teuben, P., & Wahhaj, Z. 2006, *The Astrophysical Journal*, 649, L37
- Cabrit, S., & Bertout, C. 1990, *Astrophys. J.*, 348, 530
- Cazzoli, G., Pizzarini, C., & Lapinov, A. 2003, *Astrophys. J. Letters*, 592, L95
- Chabrier, G., Baraffe, I., Allard, F., & Hauschildt, P. 2000, *Astrophys. J.*, 542, 464
- Chen, X., Arce, H. G., Zhang, Q., Bourke, T. L., Launhardt, R., Schmalzl, M., & Henning, T. 2010, *The Astrophysical Journal*, 715, 1344
- Crapsi, A., Caselli, P., Walmsley, C., Myers, P., Tafalla, M., Lee, C., & Bourke, T. 2005a, *Astrophys. J.*, 619, 379

- Crapsi, A., DeVries, C. H., Huard, T. L., Lee, J.-E., Myers, P. C., Ridge, N. A., Bourke, T. L., Evans, N. J., Jørgensen, J. K., Kauffmann, J., Lee, C. W., Shirley, Y. L., & Young, C. H. 2005b, *Astronomy and Astrophysics*, 439, 1023
- de Gregorio-Monsalvo, I., Gomez, J. F., Suarez, O., Kuiper, T. B. H., Rodriguez, L. F., & JimenezBailon, E. 2006, *The Astrophysical Journal*, 642, 319
- di Francesco, J., Evans II, N., Caselli, P., Myers, P., Shirley, Y., Aikawa, Y., & Tafalla, M. 2007, in *Protostars and Planets V*, ed. B. Reipurth, D. Jewitt, & K. Keil, 17–32
- Dore, L., Caselli, P., Beninati, S., Bourke, T., Myers, P., & Cazoli, G. 2004, *Astron. & Astrophys.*, 413, 1177
- Dunham, M., Crapsi, A., Evans II, N., Bourke, T., Huard, T., Myers, P., & Kauffmann, J. 2008, *Astrophys. J. Suppl.*, 179, 249
- Dunham, M., Evans II, N., Bourke, T., Dullemond, C., Young, C., Brooke, T., Chapman, N., Myers, P., Porras, A., Spiesman, W., Teuben, P., & Wahhaj, Z. 2006, *Astrophys. J.*, 651, 945
- Dunham, M. M., Evans, N. J., Bourke, T. L., Myers, P. C., Huard, T. L., & Stutz, A. M. 2010a, *The Astrophysical Journal*, 721, 995
- Dunham, M. M., Evans, N. J., Terebey, S., Dullemond, C. P., & Young, C. H. 2010b, *The Astrophysical Journal*, 710, 470
- Ebert, R. 1955, *Zeitschrift für Astrophysics*, 37, 217
- Elston, R. 1998, in *Proc. SPIE Vol. 3354*, p. 404–413, *Infrared Astronomical Instrumentation*, Albert M. Fowler; Ed., ed. A. Fowler, 404–413
- Enoch, M. L., Lee, J.-E., Harvey, P., Dunham, M. M., & Schnee, S. 2010, *The Astrophysical Journal*, 722, L33
- Evans, N., Allen, L., Blake, G., Boogert, A., Bourke, T., Harvey, P., Kessler, J., Koerner, D., Lee, C., Mundy, L., Myers, P., Padgett, D., Pontoppidan, K., Sargent, A., Stapelfeldt, K., van Dishoeck, E., Young, C., & Young, K. 2003, *Publ. Astron. Soc. Pac.*, 115, 965
- Evans, N., Harvey P.~M., Dunham, M., Huard, T., Mundy, L., Lai, S.-P., Chapman, N., Brooke, T., Enoch, M., & Stapelfeldt, K. 2007, *Spitzer Science Center Document*
- Evans, N. J., Dunham, M. M., Jørgensen, J. K., Enoch, M. L., Merín, B., van Dishoeck, E. F., Alcalá, J. M., Myers, P. C., Stapelfeldt, K. R., Huard, T. L., Allen, L. E., Harvey, P. M., van Kempen, T., Blake, G. A., Koerner, D. W., Mundy, L. G., Padgett, D. L., & Sargent, A. I. 2009, *Astrophys. J. Suppl.*, 181, 321
- Francesco, J. D., Johnstone, D., Kirk, H., MacKenzie, T., & Ledwosinska, E. 2008, *Astrophys. J. Suppl.*, 175, 277
- Gottlieb, C., Myers, P., & Thaddeus, P. 2003, *Astrophys. J.*, 588, 655
- Greaves, J., Holland, W., & Pound, M. 2003, *Monthly Not. Roy. Astron. Soc.*, 346, 441
- Heithausen, A., & Böttner, C. 2010, eprint arXiv:1010.0543
- Huard, T., Myers, P., Murphy, D., Crews, L., Lada, C., Bourke, T., Crapsi, A., Evans, N., McCarthy, D., & Kulesa, C. 2006, *Astrophys. J.*, 640, 391
- Indebetouw, R., Mathis, J., Babler, B., Meade, M., Watson, C., Whitney, B., Wolff, M., Wolfire, M., Cohen, M., Bania, T., Benjamin, R., Clemens, D., Dickey, J., Jackson, J., Kobulnicky, H., Marston, A., Mercer, E., Stauffer, J., Stolovy, S., & Churchwell, E. 2005, *Astrophys. J.*, 619, 931
- Kauffmann, J., Bertoldi, F., Bourke, T., Evans II, N., & Lee, C. 2008, *Astron. & Astrophys.*, 487, 993
- Kauffmann, J., Bertoldi, F., Evans, N., & the C2D Collaboration. 2005, *Astronomische Nachrichten*, 326, 878
- Kenyon, S. J., Hartmann, L. W., Strom, K. M., & Strom, S. E. 1990, *The Astronomical Journal*, 99, 869
- Kirk, J., Ward-Thompson, D., & André, P. 2005, *Monthly Not. Roy. Astron. Soc.*, 360, 1506
- Kirk, J., Ward-Thompson, D., Di Francesco, J., Bourke, T., Evans II, N., Merín, B., Allen, L., Cieza, L., Dunham, M., Harvey, P., Huard, T., Jørgensen, J., Miller, J., Noriega-Crespo, A., Peterson, D., Ray, T., & Rebull, L. 2009, *ArXiv e-prints*
- Kun, M. 1998, *Astrophys. J. Suppl.*, 115, 59
- Lada, C. 1987, in *IAU Symp. 115: Star Forming Regions*, 1–15
- Larson, R. B. 1969, *Monthly Notices of the Royal Astronomical Society*, 145
- Lee, C., Myers, P., & Plume, R. 2004, *Astrophys. J. Suppl.*, 153, 523
- Lee, C., Myers, P., & Tafalla, M. 1999, *Astrophys. J.*, 526, 788
- . 2001, *Astrophys. J. Suppl.*, 136, 703
- Lee, C. W., Bourke, T. L., Myers, P. C., Dunham, M., Evans, N., Lee, Y., Huard, T., Wu, J., Gutermuth, R., Kim, M.-R., & Kang, H. W. 2009, *The Astrophysical Journal*, 693, 1290
- Leung, C., & Brown, R. 1977, *Astrophys. J. Letters*, 214, L73
- Levreault, R. 1988, *Astrophys. J. Suppl.*, 67, 283
- Luhman, K., Mamajek, E., Allen, P., Muench, A., & Finkbeiner, D. 2009, *Astrophys. J.*, 691, 1265
- Luhman, K. L., & Mamajek, E. E. 2010, *The Astrophysical Journal*, 716, L120
- Maheswar, G., Lee, C. W., Bhatt, H. C., Mallik, S. V., & Dib, S. 2010, *Astronomy and Astrophysics*, 509, A44
- Mardones, D., Myers, P., Tafalla, M., Wilner, D., Bachiller, R., & Garay, G. 1997, *Astrophys. J.*, 489, 719
- Moshir, M., & al., E. 1990, in *IRAS Faint Source Catalogue, version 2.0 (1990)*, 0–+
- Motte, F., & André, P. 2001, *Astron. & Astrophys.*, 365, 440
- Müller, H., Schlöder, F., Stutzki, J., & Winnewisser, G. 2005, *JMoSt*, 742, 215
- Myers, P., Fuller, G., Mathieu, R., Beichman, C., Benson, P., Schild, R., & Emerson, J. 1987, *Astrophys. J.*, 319, 340
- Nutter, D., Stamatellos, D., & Ward-Thompson, D. 2009, *Monthly Not. Roy. Astron. Soc.*, 396, 1851
- Ott, M., Witzel, A., Quirrenbach, A., Krichbaum, T. P., Standke, K. J., Schalinski, C. J., & Hummel, C. A. 1994, *Astronomy and Astrophysics (ISSN 0004-6361)*, 284, 331
- Papovich, C., Dole, H., Egami, E., Le Floch, E., PerezGonzalez, P. G., AlonsoHerrero, A., Bai, L., Beichman, C. A., Blaylock, M., Engelbracht, C. W., Gordon, K. D., Hines, D. C., Misselt, K. A., Morrison, J. E., Mould, J., Muzerolle, J., Neugebauer, G., Richards, P. L., Rieke, G. H., Rieke, M. J., Rigby, J. R., Su, K. Y. L., & Young, E. T. 2004, *The Astrophysical Journal Supplement Series*, 154, 70
- Péault, M. 1987, *Ph.D. Thesis*
- Phan-Bao, N., Riaz, B., Lee, C.-F., Tang, Y.-W., Ho, P., Martín, E., Lim, J., Ohashi, N., & Shang, H. 2008, *Astrophys. J. Letters*, 689, L141
- Pillai, T., Wyrowski, F., Menten, K., & Krügel, E. 2006, *Astron. & Astrophys.*, 447, 929
- Radigan, J., Lafrenière, D., Jayawardhana, R., & Doyon, R. 2009, *The Astrophysical Journal*, 698, 405
- Reach, W., Faied, D., Rho, J., Boogert, A., Tappe, A., Jarrett, T., Morris, P., Cambrésy, L., Palla, F., & Valdetaro, R. 2009, *Astrophys. J.*, 690, 683
- Reiners, A., Basri, G., & Mohanty, S. 2005, *Astrophys. J.*, 634, 1346
- Santiago-García, J., Tafalla, M., Johnstone, D., & Bachiller, R. 2009, *Astronomy and Astrophysics*, 495, 169
- Scaife, A. M. M., Curtis, E. I., Davies, M., Franzen, T. M. O., Grainge, K. J. B., Hobson, M. P., Hurley-Walker, N., Lasenby,

- A. N., Olamaie, M., Pooley, G. G., Rodríguez-González, C., Saunders, R. D. E., Schammel, M., Scott, P. F., Shimwell, T., Titterton, D., Waldrum, E., & Zwart, J. T. L. 2010
- Schmid-Burgk, J., Muters, D., Müller, H. S. P., & Brupbacher-Gatehouse, B. 2004, *Astron. & Astrophys.*, 419, 949
- Shu, F. 1977, *Astrophys. J.*, 214, 488
- Skrutskie, M., Cutri, R., Stiening, R., Weinberg, M., Schneider, S., Carpenter, J., Beichman, C., Capps, R., Chester, T., Elias, J., Huchra, J., Liebert, J., Lonsdale, C., Monet, D., Price, S., Seitzer, P., Jarrett, T., Kirkpatrick, J., Gizis, J., Howard, E., Evans, T., Fowler, J., Fullmer, L., Hurt, R., Light, R., Kopan, E., Marsh, K., McCallon, H., Tam, R., Van Dyk, S., & Wheelock, S. 2006, *Astron. J.*, 131, 1163
- Sohn, J., Lee, C., Lee, H., Park, Y.-S., Myers, P., Lee, Y., & Tafalla, M. 2004, *Journal of Korean Astronomical Society*, 37, 261
- Stecklum, B., Melnikov, S., & Meusinger, H. 2007, *Astron. & Astrophys.*, 463, 621
- Straizys, V., Cernis, K., Kazlauskas, A., & Meistas, E. 1992, *Baltic Astronomy*, 1, 149
- Tachihara, K., Rengel, M., Nakajima, Y., Yamaguchi, N., André, P., Neuhäuser, R., Onishi, T., Fukui, Y., & Mizuno, A. 2007, *Astrophys. J.*, 659, 1382
- Weingartner, J., & Draine, B. 2001, *Astrophys. J.*, 548, 296
- Whitney, B., Wood, K., Bjorkman, J., & Cohen, M. 2003, *Astrophys. J.*, 598, 1079
- Winnewisser, G., Belov, S., Klaus, T., & Schieder, R. 1997, *Journal of Molecular Spectroscopy*, 184, 468
- Wu, J., Dunham, M., Evans II, N., Bourke, T., & Young, C. 2007, *Astron. J.*, 133, 1560
- Wu, Y., Wei, Y., Zhao, M., Shi, Y., Yu, W., Qin, S., & Huang, M. 2004, *Astron. & Astrophys.*, 426, 503
- Wuchterl, G., & Tscharnuter, W. 2003, *Astron. & Astrophys.*, 398, 1081
- Young, C., Jørgensen, J., Shirley, Y., Kauffmann, J., Huard, T., Lai, S., Lee, C., Crapsi, A., Bourke, T., Dullemond, C., Brooke, T., Porras, A., Spiesman, W., Allen, L., Blake, G., Evans, N., Harvey, P., Koerner, D., Mundy, L., Myers, P., Padgett, D., Sargent, A., Stapelfeldt, K., van Dishoeck, E., Bertoldi, F., Chapman, N., Cieza, L., DeVries, C., Ridge, N., & Wahhaj, Z. 2004, *Astrophys. J. Suppl.*, 154, 396

## APPENDIX A: PHOTOMETRY FOR L1148–IRS

Table A1 presents the SED of L1148–IRS, compiled from data sources listed in Section 4.1. Here we give some further processing details.

In the IRAC and the MIPS1 band, we average results, if more than one flux density measurement is available. For the MIPS2 and MIPS3 band, we use our own aperture photometry results instead of the values derived by point–source fitting; this is likely to be better suited for the slightly extended emission. The SHARC–II and SCUBA upper limits are derived by adding the observed flux and the noise level times three (our SHARC–II limits supersede those from Wu et al. 2007). We check our photometry against further Spitzer MIPS (Kirk et al. 2009) and independent Akari (Nutter et al. 2009) studies of the region<sup>7</sup>. The data are usually consistent within their uncertainties. A notable exception is the Akari

flux of 130 mJy at 90  $\mu$ m wavelength; this is inconsistent with the much higher MIPS flux densities at 70 and 160  $\mu$ m. We have no explanation for this, but elect to rely on our higher quality Spitzer data.

## APPENDIX B: THE L1148 DENSE CORE

As already explained in Section 2.1, Kauffmann et al. (2005) lacked the space to describe their data in detail. To provide a proper reference, we do therefore present those observations in this appendix. We also discuss new observations of contraction motions in L1148 (Appendix B5). To improve the readability of this paper, their rather straightforward discussion is removed from the main text.

In this appendix, we do therefore first introduce a previously rather undocumented data set that had never been documented well, i.e., our Effelsberg observations (Appendix B1). We then discuss the spatial mass distribution of the core in more detail than appropriate in the main text (Appendix B2). This is followed by extended discussions of the line emission data first used by Kauffmann et al. (2005) (Appendix B3: velocity field of the cloud; Appendix B4: molecular abundances). We finish with an analysis of new data on contraction motions in the cloud (Appendix B5).

### B1 Additional Data: Effelsberg 100m–telescope

Spectroscopic observations with the Effelsberg 100m–telescope (operated by the Max–Planck–Institut für Radioastronomie in Bonn, Germany) were done 2005 April 13 and April 29 to May 2. The ( $J, F = 2, 1-1, 0$ ) transition of CCS was observed with the facility 1.3 cm primary focus spectral line receiver and the AK90 autocorrelator as the backend. All data was taken in the frequency switching mode. The pointing corrections in azimuth and elevation were mostly below 6'', but corrections of 15'' occurred once. The focus corrections were below 0.6 mm. Pointing was checked at least once in 4 hours and the focus corrected at least once in 6 hours. Further details are listed in Table B1.

The spectroscopic observations were reduced using CLASS. We removed low–order baselines and partially used Fourier (FFT) filtering to further improve the baseline quality. Further details of the data reduction are given in the respective sections below.

The data were calibrated using cross–scans towards 3C48, 3C123, 3C147, 3C286, and NGC7027. The observed telescope response is combined with the flux densities given by Ott et al. (1994) to determine the calibration factor. We use a factor of 3.62 to convert the dimensionless telescope counts into main beam brightness temperature. Please refer to `\protect\vrulewidth0pt\protect\href{http://www.mpifr-bonn.mpg.de/staff/tpillai/eff_calib/eff_calib.html}{http://www.mpifr-bonn.mpg.de/staff/tpillai/eff_calib/eff_calib.html}` for more details.

### B2 Spatial Mass Distribution

Based on the dust emission maps shown in Figures 1 and 2, Kauffmann et al. (2008) noted that the L1148 region contains two parallel filaments of 3  $M_{\odot}$  and 9  $M_{\odot}$ , respectively of  $1' \times 5'$  size

his Akari study (Nutter et al. 2009). We are grateful to him and J. Kirk for providing us their results in advance of publication.

<sup>7</sup> D. Nutter provided us with dedicated photometry, based on the data from

**Table A1.** The spectral energy distribution of L1148–IRS

Band	Wave Length $\mu\text{m}$	Bandwidth $\mu\text{m}$	Resolution arcsec	Apertures arcsec	Flux Density mJy	Calibration Uncertainty
2MASS <i>J</i>	1.24	0.16	2.8	PSF	< 0.1	2%
FLAMINGOS <i>J</i>	1.24	0.16	1.3	2.56, 6.4 – 12.8	< 0.1	2%
2MASS <i>H</i>	1.66	0.25	2.8	PSF	< 0.6	2%
FLAMINGOS <i>H</i>	1.66	0.25	1.3	2.56, 6.4 – 12.8	$0.421 \pm 0.021$	2%
2MASS $K_s$	2.16	0.26	2.8	PSF	$0.9 \pm 0.1$	2%
FLAMINGOS $K_s$	2.16	0.26	1.3	2.56, 6.4 – 12.8	$1.304 \pm 0.065$	2%
IRAC 1	3.6	0.8	1.7	PSF	1.22	15%
IRAC 2	4.5	1.0	1.7	PSF	1.33	15%
IRAC 3	5.7	1.4	1.9	PSF	0.83	15%
IRAC 4	7.9	2.9	2.0	PSF	1.14	15%
IRAS 12	12	7	25	PSF	< 77	3%
MIPS 1	24	5	6	PSF	72.5	15%
IRAS 25	25	11	25	PSF	156	6%
IRAS 60	60	33	60	PSF	283	6%
MIPS 2	71	19	18	60, 80 – 120	326	20%
IRAS 100	100	31.5	100	PSF	< 3955	10%
MIPS 3	156	35	40	48, 128 – 256	$\approx 500$	50%
SHARC–II	350	45	9	25.8	< 608	15%
SCUBA	850	170	14	22.9	< 159	20%
MAMBO	1200	210	11	25.8	33	20%

**Notes.** For every band the central wavelength and width of the filter, the telescope resolution, the apertures used for photometry, the measured flux density including color corrections (where necessary) and its uncertainty due to noise, and the calibration uncertainty are given. For most bands photometry is done by point–source fitting. Then the aperture to that the flux density refers is given by the point spread function (PSF) and we mark these bands by listing “PSF” as the used aperture. For the other bands, where we perform aperture photometry, the first number given for the aperture is the diameter across which the intensity is integrated, while the given range indicates the diameter of the inner and outer circle enclosing the area used to obtain an estimate for the background intensity (does not apply to bolometer data). The uncertainty in the MIPS 3 band reflects the flux density variation due to different aperture choices.

**Table B1.** Spectroscopic observations at the IRAM 30m–telescope and the Effelsberg 100m–telescope

Molecule	Transition	Frequency GHz	$T_{\text{mb}}$ <sup>a</sup> K	Vel. Uncert. <sup>b</sup> km s <sup>−1</sup>	Beam Size arcsec	Freq. Throw <sup>c</sup> MHz	$T_{\text{sys}}$ <sup>d</sup> K	Vel. Resol. <sup>e</sup> km s <sup>−1</sup>
<i>Effelsberg:</i>								
CCS	$J, F = 2, 1-1, 0$	22.3440308 <sup>1</sup>	$1.43 \pm 0.32$	0.013	39	2.5	271	0.033
<i>IRAM 30m-telescope:</i>								
N <sub>2</sub> H <sup>+</sup>	$J, F_1, F =$ 1, 0, 1–0, 1, 2	93.1762608 <sup>2</sup>	$0.27 \pm 0.05$	0.019	26	7.0	142 <sup>f</sup> 196 <sup>g</sup>	0.063 <sup>f</sup> 0.021 <sup>g</sup>
N <sub>2</sub> D <sup>+</sup>	$J, F_1, F =$ 1, 0, 1–0, 1, 2	77.1121180 <sup>2</sup>	< 0.21	0.023	31	7.8	267	0.076
CS	$J = 2-1$ $J = 3-2$	97.980953 <sup>3</sup> 146.969029 <sup>3</sup>	$0.30 \pm 0.04$ < 0.22	0.006 0.002	25 16	7.0 5.0	145 363	0.020 0.040
<sup>12</sup> CO	$J = 2-1$	230.538000 <sup>4</sup>	$4.87 \pm 0.14$	0.001	10	15	377 <sup>f</sup>	0.051 <sup>f</sup>
C <sup>18</sup> O	$J = 2-1$	219.560358 <sup>5</sup>	$1.00 \pm 0.10$	0.001	11	15	291	0.053
HCO <sup>+</sup>	$J = 1-0$	89.1884957 <sup>1</sup>	$0.64 \pm 0.04$	0.037	27	7.0	132	0.023
H <sup>13</sup> CO <sup>+</sup>	$J = 1-0$ “primary”	86.7542982 <sup>6</sup>	$0.20 \pm 0.04$	0.014	28	7.0	111	0.045
HCN	$J, F = 1, 1-0, 1$ $J, F = 1, 2-0, 1$ $J, F = 1, 0-0, 1$	88.6304157 <sup>1</sup> 88.6318473 <sup>1</sup> 88.6339360 <sup>1</sup>	$0.05 \pm 0.02$ $0.16 \pm 0.02$ $0.09 \pm 0.02$	0.003 ..... ditto ..... ditto	27 ..... .....	7.0 ..... .....	131 ..... .....	0.066 ..... .....

**References.** (1) Müller et al. (2005); (2) Dore et al. (2004); (3) Gottlieb et al. (2003); (4) Winnewisser et al. (1997); (5) Cazzoli et al. (2003); (6) Schmid-Burgk et al. (2004)

**Notes.** <sup>a</sup> peak main beam brightness temperature per spectrum (and noise level measured as the root mean square deviation at velocities free of line emission) at the position closest to L1148–IRS, determined using Gaussian fits to the lines, where dashes (“–”) indicate non-detections, and upper limits are the noise level times three; <sup>b</sup> uncertainty in frequency, and implied uncertainty in velocity; <sup>c</sup> frequency throw in frequency–switched observations; <sup>d</sup> system temperature, in main beam brightness scale; <sup>e</sup> velocity resolution of the spectral observations, after smoothing if applicable; <sup>f</sup> for mapping observations in December 2004; <sup>g</sup> for pointed observations in July 2005



(i.e.,  $0.1 \times 0.5 \text{ pc}^2$ ; both filaments have a similar size). The north-western filament contains L1148-IRS and has the lower mass. The  $\text{H}_2$  peak column densities are  $6 \times 10^{21} \text{ cm}^{-2}$  and  $8 \times 10^{21} \text{ cm}^{-2}$ .

To derive radial density laws, we execute a new analysis of cuts through the dust emission peak near L1148-IRS. They are taken at a position angle 135 deg, i.e., perpendicular to the filament axis. The cuts (i.e., dust emission intensity as a function of offset from the peak) are compared to intensity profiles expected for density laws  $\rho(r) \propto r^{-\alpha}$  and constant dust temperature. The synthetic intensities are calculated taking the limited telescope resolution into account. Within the uncertainties, the dust emission distribution is consistent with pure power-laws with  $\alpha = 1.75$  to 2.0. In other words, compared to the beam diameter, regions of constant density (i.e.,  $\alpha = 0$ ) cannot have a significant size.

### B3 Velocity Field

Kauffmann et al. (2005) used CCS ( $J_F = 2_1-1_0$ ) maps (not repeated here) to gauge the velocity field of the L1148 region on very large spatial scales (i.e.,  $\gg 1'$ , or  $\gg 0.1 \text{ pc}$ ). The maps reveal similar velocities  $\sim 2.7 \text{ km s}^{-1}$  for the two dust filaments (that are traced by the CCS intensity), and full width at half maximum (FWHM) line widths (from Gaussian fits) of 0.15 to 0.25  $\text{km s}^{-1}$ . There is a velocity gradient along the north-western dust filament harboring L1148-IRS: the filament's north-eastern edge (that contains L1148-IRS) has a velocity 2.63  $\text{km s}^{-1}$ , while the south-western end moves with 2.78  $\text{km s}^{-1}$ . This difference of 0.15  $\text{km s}^{-1}$  is similar to the line width, and thus rather significant. The transition from “low” to “high” velocity occurs rather abruptly, i.e., over a distance of only  $\approx 1'$ , or  $\approx 0.1 \text{ pc}$ . This suggests that this filament actually consists of two physically independent objects that form a single object only in projection. The line width is slightly elevated in the transition region, but not to a level which would clearly indicate the physical interaction of the two velocity components (e.g., not by a multiple of the average line width). The transition zone lies only  $\approx 1'$  to the south-east of L1148-IRS, and is thus relatively close to our target object.

In the maps of Kauffmann et al. (2005), smaller spatial scales are well probed by the  $\text{C}^{18}\text{O}$  ( $J = 2-1$ ) maps of size  $100'' \times 100''$ , or  $(0.16 \text{ pc})^2$ . As shown in Figure B1, they reveal two velocity components in the immediate vicinity of L1148-IRS: one at velocities  $\sim 2.6 \text{ km s}^{-1}$ , and one at  $\sim 3.0 \text{ km s}^{-1}$ . The FWHM line widths (from Gaussian fits) show significant variation across the map; they are 0.2 to 0.5  $\text{km s}^{-1}$ , when only taking reliable fits into account. The velocity of the lower-velocity emission globally increases from north-east to the south-west, but this trend is not as distinct as seen in CCS. Interestingly, the  $\text{C}^{18}\text{O}$  integrated intensity presented in Figure B2 does not correlate with the dust intensity distribution (also see Appendix B4).

The kinematics of the very dense gas are traced by the  $\text{N}_2\text{H}^+$  ( $J = 1-0$ ) maps of Kauffmann et al. (2005). As seen in Figure B2, these cover the same region as the  $\text{C}^{18}\text{O}$  maps. The spectra show no signs of multiple velocity components. Characteristic velocities can be derived by simultaneously fitting all  $\text{N}_2\text{H}^+$  hyperfine satellites. They are of order 2.6  $\text{km s}^{-1}$ . Velocities increase from north-east ( $\sim 2.55 \text{ km s}^{-1}$ ) to south-west ( $\sim 2.63 \text{ km s}^{-1}$ ), just as seen for CCS and  $\text{C}^{18}\text{O}$ . The FWHM line widths are 0.15 to 0.25  $\text{km s}^{-1}$ , with a peak towards L1148-IRS.

The low observed line widths  $\lesssim 0.25 \text{ km s}^{-1}$  are noteworthy;  $\text{N}_2\text{H}^+$  lines in supposedly “evolved” cores (Crapsi et al. 2005a), as well as CCS transitions in star-forming cores

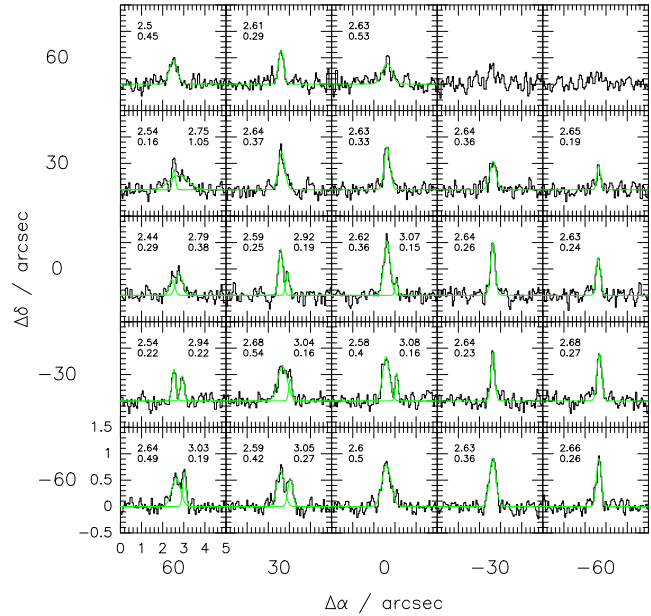


**Figure B1.** Spectra in the  $\text{C}^{18}\text{O}$   $J = 2-1$  transition towards L1148-IRS as observed with frequency switching on a  $5 \times 5$  point grid with  $30''$  spacing. Offsets are given relative to the approximate dust emission peak position ( $\alpha = 20^{\text{h}}40^{\text{m}}56^{\text{s}}.5$ ,  $\delta = +67^{\circ}22'58''.0$  [J2000.0]). The LSR velocity and intensity in the  $T_{\text{mb}}$ -scale are shown for the spectrum in the lower left corner. Gaussian fits to velocity components are drawn for those positions where the component identification is obvious. Small numbers give for every component fitted the derived LSR velocities (upper lines) and line width (lower lines; both in  $\text{km s}^{-1}$ ).

(de Gregorio-Monsalvo et al. 2006), are observed to typically have lines wider than 0.25  $\text{km s}^{-1}$ . It is, e.g., possible that the wide lines in non-VeLLO cores are a manifestation of large-scale rapid inward motions associated with accretion on forming stars. If these motions are slower in VeLLO cores, or their spatial extent is smaller, then it would be understandable why VeLLO cores have so narrow lines. However, in the light of the present data situation, any such consideration remains speculative.

### B4 Molecular Abundances

The CCS integrated intensity does not correlate well with the dust emission (Figure 3 of Kauffmann et al. 2005). In contrast,  $\text{N}_2\text{H}^+$  ( $1-0$ ) emission (Figure B2) traces the core very well.

The correlation between the  $\text{C}^{18}\text{O}$  ( $2-1$ ) emission and the dust distribution is unusually weak (Figure B2): while the dust emission filament runs NE-SW, the  $\text{C}^{18}\text{O}$  emission features a distinct wedge that starts near L1148-IRS and flares towards SSE (position angle roughly  $160^\circ$ ). This structure is part of the aforementioned lower-velocity  $\text{C}^{18}\text{O}$  component: it is still seen if subtracting the emission from the higher-velocity component from the map (by using the fits shown in Figure B1).

Kauffmann et al. (2005) calculate abundances using the procedures and molecular constants laid out by Crapsi et al. (2005a); for  $\text{N}_2\text{H}^+$ , optical depths and excitation temperatures are derived from hyperfine-fits, while  $\text{C}^{18}\text{O}$  lines are assumed to be optically thin and to have an excitation temperature of 10 K. Under these assumptions, the CO depletion factor (which is supposed to increase when CO freezes out onto dust),  $f_{\text{d}} = [N(\text{C}^{18}\text{O})/N(\text{H}_2)]_0/[N(\text{C}^{18}\text{O})/N(\text{H}_2)]_{\text{obs}}$ , is calculated from

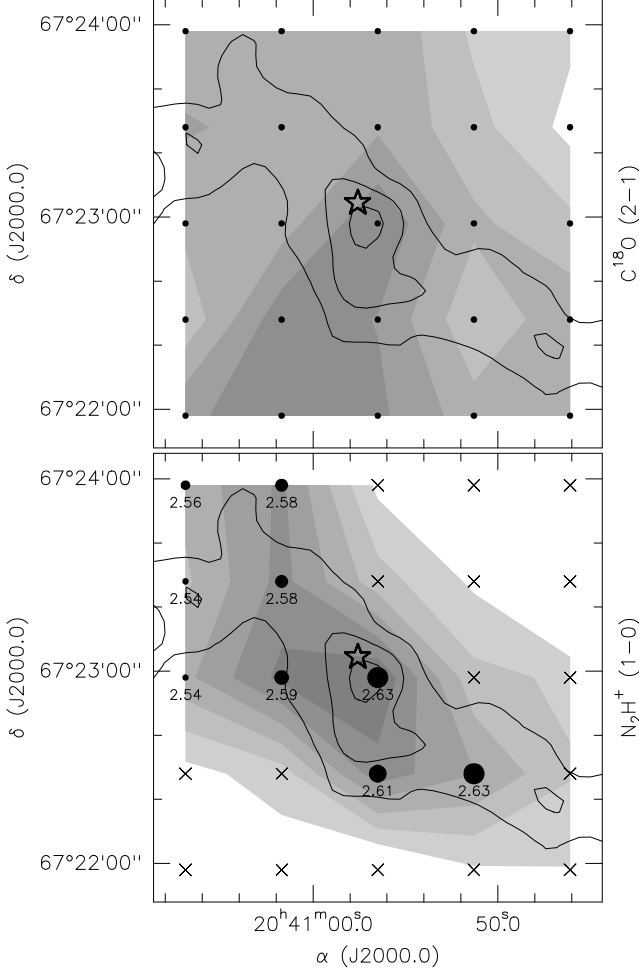


**Figure B2.** Maps of  $\text{C}^{18}\text{O}$  ( $J = 2-1$ ) and  $\text{N}_2\text{H}^+$  ( $J = 1-0$ ) integrated intensity. Grid markers give the positions observed in our study. Shading illustrates the intensities recorded during the observations. Contours outline the dust emission detected by MAMBO. For  $\text{N}_2\text{H}^+$ , marker sizes and numbers indicate the radial velocity derived from hyperfine fitting; crosses are drawn if the emission is too faint to be fitted reliably. A star marks the position of L1148-IRS.

the observed (subscript ‘obs’) and “canonic” (‘0’) dust and CO column densities,  $N$ , as

$$f_d = 0.42 \left( \frac{S_{1.2\text{ mm}}^{\text{beam}}}{\text{mJy beam}^{-1}} \right) \left( \frac{\int T_{\text{mb}}(\text{C}^{18}\text{O}[2-1]) dv}{\text{K km s}^{-1}} \right)^{-1}, \quad (\text{B1})$$

where  $S_{1.2\text{ mm}}^{\text{beam}}$  is the dust emission intensity (per  $11''$  beam), and  $\int T_{\text{mb}}(\text{C}^{18}\text{O}[2-1]) dv$  is the velocity-integrated  $\text{C}^{18}\text{O}$  intensity in  $T_{\text{mb}}$ -scale. Note that Kauffmann et al. (2005) use — in deviation to all other parts of this paper — dust emission intensity-to-mass conversion factors from Crapsi et al. (2005a) instead of those suggested by Kauffmann et al. (2008). This scheme is adopted to make our depletion factors more comparable to those of Crapsi et al.. If one were to use the Kauffmann et al. recommendations,  $f_d$  would decrease by a factor 2.54. Comparison shows that this approach typically overestimates the Crapsi et al. (2005a; their Table 6) estimates from (1-0) line data by a factor of 1.3, probably because of different excitation conditions for the (1-0) and (2-1) lines and differences in beam matching (for the present data, the beam in  $\text{C}^{18}\text{O}$  observations is smaller than the one in the smoothed MAMBO maps used to get  $S_{1.2\text{ mm}}^{\text{beam}}$ ).

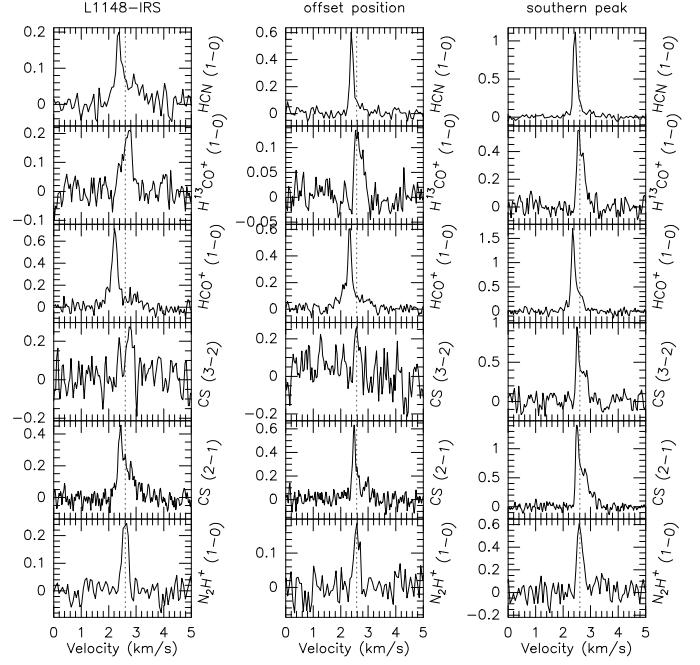


**Figure B3.** Spectra towards the positions (left to right) and transitions (top to bottom;  $J, F = 1, 2-0, 1$  for HCN,  $J, F_1, F = 1, 0, 1-0, 1, 2$  for  $\text{N}_2\text{H}^+$ ) defined in Table B2. Dotted vertical lines indicate the systemic velocity derived from the  $\text{N}_2\text{H}^+$  ( $J, F_1, F = 1, 0, 1-0, 1, 2$ ) transition. All well detected lines believed to be good tracers of infall have peaks blueshifted from the systemic velocity, indicating inward motions.

The CO depletion factor peaks towards L1148-IRS, where  $f_d = 7.8 \pm 1.3$ . Compared to other dense cores, this is relatively low, in particular since this approach is likely to overestimate the true value (see above). For the same position, an  $\text{N}_2\text{H}^+$  column density of  $(3.1 \pm 0.6) \times 10^{12} \text{ cm}^{-2}$  is derived from deep new integrations to probe contraction motions (Appendix B5). We do not detect significant  $\text{N}_2\text{D}^+$  emission. Assuming that the lines are optically thin, we derive  $\text{N}_2\text{D}^+$  column densities  $< 0.5 \times 10^{12} \text{ cm}^{-2}$  (using the intensity noise level times three).

## B5 Contraction Motions

The systemic reference velocity of the dense core,  $v_{\text{ref}}$ , can be well measured using the optically thin  $J, F_1, F = 1, 0, 1-0, 1, 2$  transition of the  $\text{N}_2\text{H}^+$  dense gas tracer. Towards L1148-IRS, we derive a velocity of  $2.60 \text{ km s}^{-1}$  (Table B2). Many supposedly optically thick lines do, however, peak at lower velocities (Figure B3), i.e. they are blue-shifted. Such velocity shifts are characteristic of dense cores undergoing contraction (Leung & Brown 1977). The velocity offset of a line peaking at velocity  $v_i$  can be characterized using dimensionless velocity differences,

$$\delta v_i = \frac{v_i - v_{\text{ref}}}{\Delta v_{\text{ref}}} \quad (\text{B2})$$

(Mardones et al. 1997), where  $\Delta v$  is the line width at half peak intensity. If  $\delta v_i < 0$ , then the line is blue-shifted, which suggests contraction motions. Expansion implies  $\delta v_i > 0$ .

Table B2 gives observed peak velocities in L1148. These are derived by fitting Gaussian lines to the peaks (and sometimes additional Gaussians to the base). Table B3 gives the corresponding dimensionless velocity differences. As outlined in Figure 2, we searched three positions for contraction motions, in order to remove

**Table B2.** Line Velocities and Widths for several Transitions observed towards selected Positions.

Line	L1148–IRS		offset position		southern peak	
	20 <sup>h</sup> 40 <sup>m</sup> 56 <sup>s</sup> .5, +67°22′58″.0	$v_{\text{LSR}}/\text{km s}^{-1}$ $\Delta v/\text{km s}^{-1}$	20 <sup>h</sup> 41 <sup>m</sup> 01 <sup>s</sup> .7, +67°23′28″.0	$v_{\text{LSR}}/\text{km s}^{-1}$ $\Delta v/\text{km s}^{-1}$	20 <sup>h</sup> 41 <sup>m</sup> 14 <sup>s</sup> .0, +67°20′31″.5	$v_{\text{LSR}}/\text{km s}^{-1}$ $\Delta v/\text{km s}^{-1}$
N <sub>2</sub> H <sup>+</sup> ( $J, F_1, F = 1, 0, 1-0, 1, 2$ )	2.602 ± 0.015	0.244 ± 0.030	2.583 ± 0.023	0.232 ± 0.048	2.614 ± 0.013	0.243 ± 0.029
CS ( $J = 2-1$ )	2.418 ± 0.005	0.149 ± 0.017	2.488 ± 0.003	0.118 ± 0.010	2.509 ± 0.002	0.119 ± 0.004
CS ( $J = 3-2$ )					2.513 ± 0.005	0.106 ± 0.015
HCO <sup>+</sup> ( $J = 1-0$ )	2.218 ± 0.001	0.204 ± 0.013	2.327 ± 0.003	0.119 ± 0.008	2.356 ± 0.002	0.115 ± 0.006
H <sup>13</sup> CO <sup>+</sup> ( $J = 1-0$ )	2.681 ± 0.016	0.420 ± 0.038	2.652 ± 0.015	0.314 ± 0.028	2.628 ± 0.008	0.293 ± 0.017
HCN ( $J, F = 1, 2-0, 1$ )	2.360 ± 0.013	0.197 ± 0.048	2.398 ± 0.006	0.127 ± 0.018	2.424 ± 0.008	0.125 ± 0.021
HCN ( $J, F = 1, 1-0, 1$ )			2.429 ± 0.018	0.198 ± 0.046	2.438 ± 0.012	0.113 ± 0.032
HCN ( $J, F = 1, 0-0, 1$ )	2.601 ± 0.041	0.566 ± 0.086	2.460 ± 0.016	0.153 ± 0.033	2.469 ± 0.010	0.124 ± 0.034

**Notes.** The observations hold for the J2000.0 positions defined in the header. These are also marked in Figure 2. If more than one line has to be fitted simultaneously to achieve a good fit to the narrow peak and the broad base of a line, then the parameters for the component with the lower velocity are listed. No numbers are given for transitions not detected well enough to allow fitting. The lines believed to be optically thick all peak at velocities below the systemic one derived from N<sub>2</sub>H<sup>+</sup>.

**Table B3.** Dimensionless Velocity Shifts towards selected Positions

Line	$\delta v_i = (v_i - v_{\text{N}_2\text{H}^+})/\Delta v_{\text{N}_2\text{H}^+}$		
	L1148–IRS	offset position	southern peak
CS			
$J = 2-1$	−0.75 ± 0.09	−0.41 ± 0.08	−0.43 ± 0.05
$J = 3-2$			−0.42 ± 0.05
HCO <sup>+</sup>			
$J = 1-0$	−1.57 ± 0.19	−1.10 ± 0.23	−1.06 ± 0.13
H <sup>13</sup> CO <sup>+</sup>			
$J = 1-0$	0.32 ± 0.04	0.30 ± 0.06	0.06 ± 0.01
HCN			
$J, F = 1, 2-0, 1$	−0.99 ± 0.12	−0.80 ± 0.16	−0.78 ± 0.09
$J, F = 1, 1-0, 1$		−0.66 ± 0.14	−0.72 ± 0.09
$J, F = 1, 0-0, 1$	0.00 ± 0.10	−0.53 ± 0.11	−0.60 ± 0.07

**Notes.** Dimensionless velocity shifts in several transitions towards the positions defined in Table B2. No numbers are given for transitions not well enough detected to allow fitting. The lines believed to be optically thick all do have negative line shifts indicative of inward motions.

biases from possible foregrounds to L1148. All lines are supposedly optically thick. This only excludes the “isolated” N<sub>2</sub>H<sup>+</sup> hyperfine satellite (i.e.,  $J, F_1, F = 1, 0, 1-0, 1, 2$ ) and the H<sup>13</sup>CO<sup>+</sup> (1–0) transition, which can therefore work as velocity references.

All well-detected optically thick lines peak at velocities blue-shifted from the N<sub>2</sub>H<sup>+</sup> reference velocity. This only excludes the ( $F = 0-1$ ) emission of HCN towards L1148–IRS, which is a particular case discussed below. In all tracers, the dimensionless line asymmetries are largest towards L1148–IRS. This position is a “strong infall candidate”, following the criteria for CS (2–1) emission put forward by Lee et al. (1999: i.e., a CS emission peak with significant blue-shift; red-shifted emission at a brightness below the one of the blue-shifted emission; and no asymmetries in the isolated N<sub>2</sub>H<sup>+</sup> line). Also, the values of the CS and HCN line asymmetries towards L1148–IRS are unusually large for starless cores: only 18% of the CS cores probed by Lee et al. (1999), respectively 40% of the HCN cores studied in the ( $F = 2-1$ ) transition by Sohn et al. (2004), have larger asymmetries (for CS, we use the data after the reanalysis by Lee et al. 2001). Note that the asymmetry in the HCN satellites decreases with decreasing optical

depth (in LTE, the optical depth ratios for different  $F$  are 1:5:3 for [0–1]:[2–1]:[1–1]), just as expected for contracting cores. Towards L1148–IRS, the possibly optically thin  $F = 0-1$  line of HCN has an unusually large line width of 0.57 km s<sup>−1</sup>. This may hint at mechanical energy input by the YSO, for example in the form of outflows. The H<sup>13</sup>CO<sup>+</sup> (1–0) is supposedly optically thin and peaks at higher velocities than the optically thick lines. This confirms the velocity differences with respect to N<sub>2</sub>H<sup>+</sup>, although the line cannot serve as a precise velocity reference because of unresolved hyperfine substructure (Schmid-Burgk et al. 2004).

It thus appears that the natal dense core of L1148–IRS is indeed contracting. This is suggested by the negative velocity differences and the particularly strong line asymmetries towards the embedded source, L1148–IRS. The prevalence of blue-shifts throughout the L1148 region may actually indicate that the entire region (i.e., on scales larger than the  $\sim 0.3$  pc containing the three positions probed) is contracting.